

AD-A179 973

DNA-TR-85-123

THE ATMOSPHERIC EFFECTS OF SOOT RESULTING FROM A NUCLEAR CONFLICT

A. S. Endal
Applied Research Corporation
8201 Corporate Drive, Suite 920
Landover, MD 20785

20 March 1985

Technical Report

CONTRACT No. DNA 001-84-C-0318

Approved for public release;
distribution is unlimited.

THIS WORK WAS SPONSORED BY THE DEFENSE NUCLEAR AGENCY
UNDER RDT&E RMSS CODE B310084466 C99QMXWB00005 H2590D.

Prepared for
Director
DEFENSE NUCLEAR AGENCY
Washington, DC 20305-1000

4 DTIC
S ELECTED
MAY 08 1987
D
E

20030121168

87 5 7 003

**Destroy this report when it is no longer needed. Do not return
to sender.**

**PLEASE NOTIFY THE DEFENSE NUCLEAR AGENCY.
ATTN: TITL, WASHINGTON, DC 20306-1000, IF YOUR
ADDRESS IS INCORRECT, IF YOU WISH IT DELETED
FROM THE DISTRIBUTION LIST, OR IF THE ADDRESSEE
IS NO LONGER EMPLOYED BY YOUR ORGANIZATION.**



UNCLASIFIED

ADA179973

SECURITY CLASSIFICATION OF THIS PAGE

REPORT DOCUMENTATION PAGE

1a. REPORT SECURITY CLASSIFICATION UNCLASSIFIED		1b. RESTRICTIVE MARKINGS	
2a. SECURITY CLASSIFICATION AUTHORITY N/A since Unclassified		3. DISTRIBUTION/AVAILABILITY OF REPORT Approved for public release; distribution is unlimited.	
2b. DECLASSIFICATION/DOWNGRADING SCHEDULE N/A since Unclassified			
4. PERFORMING ORGANIZATION REPORT NUMBER(S) ARC Report No. 85-146		5. MONITORING ORGANIZATION REPORT NUMBER(S) DNA-TR-85-123	
6a. NAME OF PERFORMING ORGANIZATION Applied Research Corporation	6b. OFFICE SYMBOL (If applicable)	7a. NAME OF MONITORING ORGANIZATION Director Defense Nuclear Agency	
6c. ADDRESS (City, State, and ZIP Code) 8201 Corporate Drive, Suite 920 Landover, MD 20785		7b. ADDRESS (City, State, and ZIP Code) Washington, DC 20305-1000	
8a. NAME OF FUNDING/SPONSORING ORGANIZATION	8b. OFFICE SYMBOL (If applicable)	9. PROCUREMENT INSTRUMENT IDENTIFICATION NUMBER DNA 001-84-C-0318	
8c. ADDRESS (City, State, and ZIP Code)		10. SOURCE OF FUNDING NUMBERS	
		PROGRAM ELEMENT NO. 62715H	PROJECT NO. C99QMXW
		TASK NO. B	WORK UNIT ACCESSION NO. DH008536
11. TITLE (Include Security Classification) THE ATMOSPHERIC EFFECTS OF SOOT RESULTING FROM A NUCLEAR CONFLICT			
12. PERSONAL AUTHOR(S) Endal, Andrew S.			
13a. TYPE OF REPORT Technical	13b. TIME COVERED FROM 840611 TO 850211	14. DATE OF REPORT Year Month Day 850320	15. PAGE COUNT 50
16. SUPPLEMENTARY NOTATION This work was sponsored by the Defense Nuclear Agency under RDT&E RMSS Code B310084466 C99QMXWB00005 H2590D.			
17. COSATI CODES	18. SUBJECT TERMS (Continue on reverse if necessary and identify by block numbers)		
FIELD GROUP SUB-GROUP	Global Effects		
18 3 1	Climate		
4 2 1	Nuclear Winter		
19. ABSTRACT (Continue on reverse if necessary and identify by block numbers) The effect of a sunlight-absorbing, high-altitude cloud layer on meteorological conditions near the earth's surface is investigated. Such a cloud (soot) layer might be formed by fires set by blast and thermal effects from a major nuclear exchange. If the soot remains in the atmosphere for a few weeks or longer, reduction of sunlight penetrating to the ground can lead to cooling of the lower troposphere. Atmospheric response to the sunlight reduction is simulated using a two-dimensional energy balance model with diffusive energy transport. Severity and duration of the surface cooling are computed as functions of: (1) the time of year at which the soot is injected; (2) the latitudinal distribution of the soot layer; (3) the infrared absorptance of the soot particles; (4) the rate of soot removal (scavenging). Global climate models (general circulation models and energy balance models) assume that the smoke from urban fires is spread uniformly on synoptic scales within a few days			
20. DISTRIBUTION/AVAILABILITY OF ABSTRACT <input type="checkbox"/> UNCLASSIFIED/UNLIMITED <input checked="" type="checkbox"/> SAME AS RPT <input type="checkbox"/> FOR USERS		21. ABSTRACT SECURITY CLASSIFICATION UNCLASSIFIED	
22a. NAME OF RESPONSIBLE INDIVIDUAL Sandra E. Young		22b. TELEPHONE (Include Area Code) (202) 325-7042	22c. OFFICE SYMBOL DNA/CSTI

DD FORM 1473, 24 MAR

83 APR edition may be used until exhausted.

All other editions are obsolete.

SECURITY CLASSIFICATION OF THIS PAGE

UNCLASSIFIED

UNCLASSIFIED

SECURITY CLASSIFICATION OF THIS PAGE

19. ABSTRACT (Continued)

after initial injection, and that microscale and mesoscale processes do not break up or remove the soot layer. The validity of these assumptions is discussed.

Global climate models (general circulation models and energy balance models) assume that the smoke from urban fires is spread uniformly on synoptic scales within a few days after initial injection, and that microscale and mesoscale processes do not break up or remove the soot layer. The validity of these assumptions is discussed. A heuristic analysis indicates that a horizontally uniform and optically thick soot layer is thermally unstable and will break up into long vertical filaments. This process may significantly change the mean optical properties of the cloud layer and thus alter the synoptic and planetary scale effects of the soot injection. Suggestions are presented for further investigations which can reduce the large uncertainties associated with the nuclear winter problem.

SECURITY CLASSIFICATION OF THIS PAGE

UNCLASSIFIED

PREFACE

The research described in this report was carried out under Contract No. DNA 001-84-C-0318 to Applied Research Corporation. This work constitutes Phase I of a Small Business Innovative Research (SBIR) project.

The author wishes to acknowledge the assistance of Mr. John G. Mengel and Mr. Edmund M. Larson, of Applied Research Corporation, in implementing the numerical model described in this report. Useful discussions of climate issues were provided by Drs. William J. Massman, William L. Ridgway, Kenji Takano, and Anne M. Thompson of Applied Research Corporation, by Dr. Gerald R. North of NASA/Goddard Space Flight Center, and by Dr. Hans R. Rainer-Schneider of M.I.T.

Accession For	
NTIS GRA&I	<input checked="" type="checkbox"/>
DTIC TAB	<input type="checkbox"/>
Unannounced	<input type="checkbox"/>
Justification	
By _____	
Distribution/	
Availability Codes	
Dist	Avail and/or Special
A-1	



TABLE OF CONTENTS

Section		Page
	PREFACE	iii
	LIST OF ILLUSTRATIONS	v
1	INTRODUCTION	1
2	SIMULATIONS	3
3	RECOMMENDATIONS	29
4	LIST OF REFERENCES	34
APPENDIX	MATHEMATICAL PROPERTIES OF THE CLIMATE MODEL	37

LIST OF ILLUSTRATIONS

<u>Figure</u>		<u>Page</u>
1	The amplitude (in $^{\circ}$ C) of the normal seasonal cycle	9
2	The phase lag (in days) of the normal seasonal cycle	11
3	Temperature changes predicted by NCAR GCM, following injection of a uniform soot layer in a 30° to 70° N band	12
4	Temperature changes predicted by the EBM, following a springtime (22 March) injection of a uniform soot layer in a 30° to 70° N band	14
5	Temperature changes predicted by the EBM following a summer (30 June) injection of a uniform soot layer in a 30° to 70° N band	15
6	Temperature changes predicted by CCAS computer model (GCM plus ocean mixed layer), at 40 days after the layer soot/dust perturbation	17
7	Temperature changes predicted by the EBM at 40 days after perturbation, using the same soot/dust parameters as in the CCAS simulation	18
8	Temperature changes in the baseline/summer case at (a) 10 days, (b) 20 days, (c) 40 days, and (d) 80 days . .	20
9	Degree-day map for the baseline/summer case, summed over a 1-year period following the initial smoke injection	22
10	Temperature differences (perturbed minus control) at day 30 in the Case 9 simulation	26
11	Degree-day map for the Case 9 simulation, summed over a 1-year period following the initial smoke injection . .	27
12	Development of a double-diffusive instability in a uniform soot cloud	31
13	A laboratory example of double-diffusive convection produced by placing hot salty water over cool fresh water	32

SECTION I

INTRODUCTION

Three types of long-term environmental effects of nuclear weapons have been widely debated—fallout, ozone layer depletion, and climate modification. The issue of biological damage from radioactive fallout was considered in a 1975 study by the National Academy of Sciences (NAS). Their report (Reference 1) concludes that, although local fallout would constitute an immediate danger to the unsheltered population directly downwind from a target area, long-term and/or widespread effects would be minor because of atmospheric dilution of the radioactive component, leading to greatly reduced exposure levels. However, a more recent report (Reference 2) concludes that the global fallout problem may be more serious than estimated by the NAS, though typical doses would still be well below the lethal range.

The major concern of the 1975 NAS report was the effect of bomb-produced oxides of nitrogen on stratospheric ozone (Reference 3). Increased levels of ultraviolet radiation transmitted by a depleted ozone layer could be a long-term and global danger to the surviving population. However, the analysis by the NAS assumed individual weapon yields in the 1 to 20 MT range. The subsequent shift in the U.S. and Soviet arsenals to smaller and more accurate weapons has reduced this concern, since plumes from tropospheric explosions with yields below 1 MT are unlikely to rise to the height of the ozone layer (Reference 4).

The third type of effect—climate modification—has recently received a great deal of attention. In 1982, Crutzen and Birks (Reference 5) hypothesized that widespread forest fires ignited by nuclear weapons would create a thick smoke layer. This would reduce the amount of sunlight reaching the ground. In 1983, Turco, et al., (Reference 6) argued that urban fires would create an even more opaque layer of black soot, which would remain in the atmosphere for several weeks or longer. During this time, the soot could spread over much of the Northern Hemisphere. By absorbing incoming sunlight well above ground level, thus short-circuiting the normal greenhouse effect, the soot layer would lead to subfreezing surface temperatures, even in summer.

A 1985 study by the NAS (Reference 7) concludes that, although the uncertainties in the Turco, et. al., scenario are presently too large to allow a quantitative prediction, the possibility of a severe surface temperature reduction following a major nuclear conflict should be seriously

considered. Such a climate effect would damage crops and lead to increased casualties among survivors of immediate nuclear effects (Reference 2). The altered atmospheric conditions could also have synergistic effects on fallout and ozone depletion (Reference 2). In the case of a protracted conflict, reduced atmospheric transmission and increased pollutant loading would seriously impact on the effectiveness of surveillance assets and air-breathing weapons systems. For the above reasons, it is desirable to reduce the uncertainties in the climate predictions to a level where the public policy and military implications can be clearly understood.

Three types of uncertainties are associated with the climatic predictions: the nuclear exchange scenario (number and size distribution of warheads, target selection, ground bursts vs. air bursts, and ambient meteorological conditions); smoke production and injection (amount of smoke, size distribution and optical properties of smoke particles, height of the smoke plume, and aging of the smoke); and atmospheric response (radiative effects, circulation changes, smoke transport, convection and precipitation, and cloud interactions). The first type of uncertainty requires that climatic response be evaluated as a function of the type of conflict and of the time of year at which the conflict occurs. The effectiveness of any defensive systems must also be considered. The second type of uncertainty can be addressed by experimental and theoretical investigations of fire, smoke, and plume properties. The last type of uncertainty must ultimately be addressed by computer simulation, since neither natural nor controlled climate perturbations occur on the estimated scale of the nuclear war effects. In the absence of an ability to observationally verify the simulations, a residual uncertainty regarding the predicted atmospheric response will always remain. Some specific issues can, however, be addressed observationally by studies of transport and aging of smoke from natural and man-made fires.

This report is concerned with the third type of uncertainty, and concentrates on modeling problems. Section 2 describes simulations with a simple type of climate model. The simulations were carried out to demonstrate the feasibility of using this model to test atmospheric response to soot loadings. The model is used to estimate sensitivity of the predicted cooling to: (1) the season at which the soot is injected, (2) the soot scavenging rates, (3) the geographical distribution of the injected soot, and (4) the infrared properties of the soot particles. Section 3 summarizes the modeling results and provides analyses of some processes not accounted for in present atmospheric simulation codes. Of particular importance, it appears that the uniform soot layer assumed in these models is thermally unstable and will tend to break up. The Appendix provides derivations of some mathematical properties of the climate model.

SECTION 2

SIMULATIONS

Climate modeling has progressed rapidly over the past decade due, in part, to the application to climate problems of general circulation models (GCM). A GCM uses a discrete grid mesh (or the equivalent harmonic expansions) to solve the primitive equations governing dynamical circulation, radiative transfer, and some form of a hydrological cycle. A typical GCM grid has horizontal resolution of ~ 500 km and vertical resolution on the order of 1 to 10 km.

Many atmospheric processes occur on spatial scales smaller than the GCM resolution. Examples of subgrid processes include: convection, precipitation, cloud interactions, frontal zone circulations, and boundary layer effects. These processes are represented in the GCMs in highly parameterized forms. The representations contain adjustable coefficients which are "tuned" to produce a good simulation of present climatic conditions.

Climate models can be tested by comparing their predictions to recent minor climate perturbations, such as caused by volcanic dust veils, and to paleoclimates reconstructed from proxy data. Only the latter type of test involves departures from the present climate of a magnitude similar to the changes postulated to occur in the aftermath of a nuclear war. For example, a few interesting ice age experiments have been carried out, with drastic departures from the present climate (References 9 and 10). However, interpreting the results of such experiments is difficult, due both to ambiguities of the paleoclimate data base and to the inherent complexity of GCM diagnostics. The model climate generated by a GCM is often as complex and inscrutable as the real climate.

In parallel with GCM construction, a number of simpler models have been developed for sensitivity experiments. It is hoped that these models will produce climates which respond to external influences in much the same way as does the real climate. If so, their simplicity can lead to a better understanding of climate response, as well as allowing efficient evaluation of a range of scenarios. In many ways, these simpler models offer a good match to the crudeness of the present understanding of the type of perturbation which would result from a large-scale nuclear war.

One example of such a simple model is a radiative-convective model (RCM), such as used in the study by Turco, et al., (Reference 6). This type of model has excellent vertical resolution and handles radiative transfer in considerable detail but has no horizontal structure.

A different type of climate model is an energy balance model (EBM), popularized by Budyko (Reference 11) and Sellers (Reference 12), and recently reviewed by North, et al., (Reference 13). An EBM uses very simple representations of energy fluxes to examine how these fluxes interact to determine the surface temperature. Most EBMs include some horizontal resolution, so the effects of geography (land-sea fractions) are included in the models. In a sense, EBMs complement RCMs, which directly calculate energy fluxes but have no geography.

With one exception (Reference 14), EBMs have not been applied to the Turco, et. al., hypothesis. The remainder of this section describes the application of a continent-resolving EBM to estimating the climate impact of a soot layer of the type postulated to follow a major nuclear conflict.

SPECIFICATIONS OF THE MODEL

We use a two-dimensional, one-level, time-dependent EBM, of the type discussed by North, et al., (Reference 15). This model was originally developed for studying the initiation of ice ages following changes in the seasonal distribution of sunlight (due to changes in the Earth's orbit). The model predictions for this case are in excellent agreement with the regular cycles of ice ages recently discovered in the paleoclimatic data (Reference 16). The model represents the large difference in thermal response times of the land and oceans by differing heat capacities. The seasonal cycle (but not the diurnal cycle) is incorporated, so the seasonal dependence of nuclear war effects can be studied. Finally, the model is simple enough that its principal mathematical properties can be directly evaluated, and the model can be economically exercised for a variety of cases. The price paid for this convenience is that certain atmospheric processes (radiative transfer and horizontal energy advection) are treated in highly idealized forms. These simplifications can best be justified by the fact that the model does predict a climate which is a good facsimile to the real climate.

The basic energy balance equation is

$$C(\vec{r}) \frac{\partial \vec{T}(\vec{r}, t)}{\partial t} = Q a(x) S(x, t) - [A + B T(\vec{r}, t)] + D \nabla^2 \vec{T}(\vec{r}, t). \quad (1)$$

where

t = time, in years with $t = 0$ at winter solstice,

\vec{r} = geographical position (latitude and longitude),

x = sine of latitude,

$C(r)$ = heat capacity per unit area.

$T(r,t)$ = surface temperature (dependent variable).

Q = solar constant/4.

$a(x)$ = fraction of solar energy absorbed by the atmosphere-ocean system.

$S(x,t)$ = relative solar radiation distribution vs. latitude and season.

A,B = empirical infrared radiation coefficients, and

D = diffusion coefficient for horizontal energy transport.

In simple terms, Equation (1) states the energy conservation rule for a vertically averaged column of atmosphere:

$$\left(\begin{array}{l} \text{net rate} \\ \text{of heating} \end{array} \right) = \left(\begin{array}{l} \text{absorbed} \\ \text{sunlight} \end{array} \right) - \left(\begin{array}{l} \text{emitted} \\ \text{infrared} \end{array} \right) + \left(\begin{array}{l} \text{horizontally} \\ \text{transported heat} \end{array} \right)$$

The numerical coefficients in this model are derived from physical arguments (C), from measurements (Q, a, A, and B), or by "tuning" the model to reproduce the observed climatology (D). Table 1 gives the values used in the model calculations described in this report; justification for these values is discussed below.

The effective heat capacity, C, depends on the mass of air and water which is closely coupled to surface conditions. Over land, we use half the mass of a column of atmosphere (i.e., the atmosphere below the 500-mb level or roughly below 5 km altitude). Over oceans, we add in the heat capacity of the water in the wind-driven mixed layer of the ocean, taken to be uniformly 75 meters in depth.

The solar constant (radiant energy flux per unit area at the top of the sunlit atmosphere) is a directly measured quantity (Reference 17); the diurnal average is obtained by dividing the solar constant by four. The fraction of the solar energy, absorbed is taken to be a quadratic function of latitude:

$$a(x) = a_0 + a_2 x^2. \quad (2)$$

with coefficients, derived from zonally averaged measurements of direct and reflected sunlight, obtained from satellite data (Reference 18). The infrared coefficients, A and B, are likewise derived by correlating satellite measurements of out-going infrared fluxes with surface temperature (Reference 19).

Table 1. Model coefficients.

Quantity	Symbol	Value
Heat Capacity	C	land: $5.07 \times 10^6 \text{ J/m}^2/\text{^oC}$ oceans: $3.64 \times 10^3 \text{ J/m}^2/\text{^oC}$
Average Insolation	Q	340 W/m^2
Co-Albedo	a	0.75
	a	-0.18
Infrared Coefficients	A	203.3 W/m^2
	B	$2.094 \text{ W/m}^2/\text{^oC}$
Diffusion Coefficient	D	$0.35 \text{ W/m}^2/\text{^oC}$
Seasonal Cycle	S_1	-0.796
	S_2	-0.477
	S_{22}	+0.147

The diffusion coefficient is not directly related to a measurable quantity. Therefore, the value of this parameter was adjusted to obtain agreement of the predicted and observed pole-to-equator temperature difference averaged over the seasonal cycle. This is the only "tuned" parameter in the model.

For simulating the normal climate, the model is driven through the seasonal cycle by the time-varying distribution of sunlight, given by

$$S(x,t) = 1 + S_1 \cos(2\pi t) P_1(x) + (S_2 + S_{22} \cos(4\pi t)) P_2(x). \quad (3)$$

where P_1 and P_2 are the Legendre polynomials. The coefficients in this expansion were adjusted to provide a "best fit" to the more complicated exact expression for the seasonal cycle (Reference 19).

The primary mathematical properties of the model concern the e-folding time for surface cooling, when the solar heating is removed, and the conduction length scale for propagation of a local temperature perturbation. Derivations of these properties are provided in the Appendix. The results, with the coefficients in Table 1, are

Cooling Time:	$\tau = C/B$
	= 28 days for continents
	= 4.6 years for oceans

Conduction Length:	$l = D/B$
	= 4,500 km.

In terms of understanding the results of the simulation, we note that the very different (by a factor of 60) cooling times for land vs. ocean imply that continental areas will cool much faster than oceanic regions. The long conduction length implies that the stabilizing influence of the oceans will propagate well into the continents. This is in agreement with GCM results (Reference 20), which predict that the most severe temperature effects are restricted to the deepest continental interiors.

MODEL SOLUTION AND VALIDATION

To solve the energy balance equation, the spatial dimensions are first expanded into spherical harmonics:

$$\vec{T}(r,t) = \sum_{l=0}^L \sum_{m=0}^l T_{lm}(t) Y_{lm}(\vec{r}) \quad (4)$$

and

$$C(\vec{r}) = \sum_{m=0}^{2L} \sum_{n=0}^L C_m Y_m(\vec{r}) \quad (5)$$

where

$$Y_m(\vec{r}) = P_m(x) \cos(m\phi) \quad (6)$$

and ϕ is longitude. The coefficients C_m are evaluated from the specified land-sea distribution. For the results discussed in this report, we used $L = 11$, implying a $15^\circ \times 15^\circ$ spatial resolution (about 1,000 km at mid-latitudes).

Substitution of Equations (2) through (5) into Equation (1) gives a system of $(L+1)(L+2)/2$ ordinary differential equations for the mode amplitudes $T_m(t)$. These equations are integrated from prescribed initial values using a fourth-order Hamming predictor-corrector method. Temperature maps are recomposed and plotted at desired intervals. To give some feeling for the computing requirements, simulation of 1 year of climate, with temperature maps at 10-day intervals, requires ~ 30 minutes of CPU time on a VAX 11/750 computer.

The ability of the model to simulate atmospheric processes was tested in two ways. First, the predicted seasonal cycle of an unperturbed (control) model was compared to the observed cycle. This test is not redundant with the tuning process since the model was tuned to match the annual mean climate, not the seasonal variation. The second type of test involved comparisons of EBM predictions for perturbed (soot) models with results obtained from GCMs, using identical soot parameters. This is not a direct validation since the GCM results could be incorrect. However, we do not claim to be able to make predictions which are superior to the GCM results. The advantage of the EBM lies in its simplicity and its ability to economically evaluate many scenarios, with integrations covering an extended period of time.

Figure 1 compares the amplitude of the model seasonal cycle with the observed climatology, as reported by Crutcher and Meserve (Reference 21) and Taljaard, et al., (Reference 22). The observational data have been smoothed with an $L = 11$ harmonic filter (i.e., the data were analyzed as in Equation (4), and the map in the bottom panel of Figure 1 was reconstructed from the derived harmonic coefficients); this procedure sets the spatial resolution of the data equal to that of the model. Both panels clearly show the influence of land masses, with reduced heat capacity and larger seasonal amplitudes, as compared to the oceans. A closer examination indicates that the model amplitude tends to be a bit small over North America and, perhaps, somewhat too large over Eurasia.

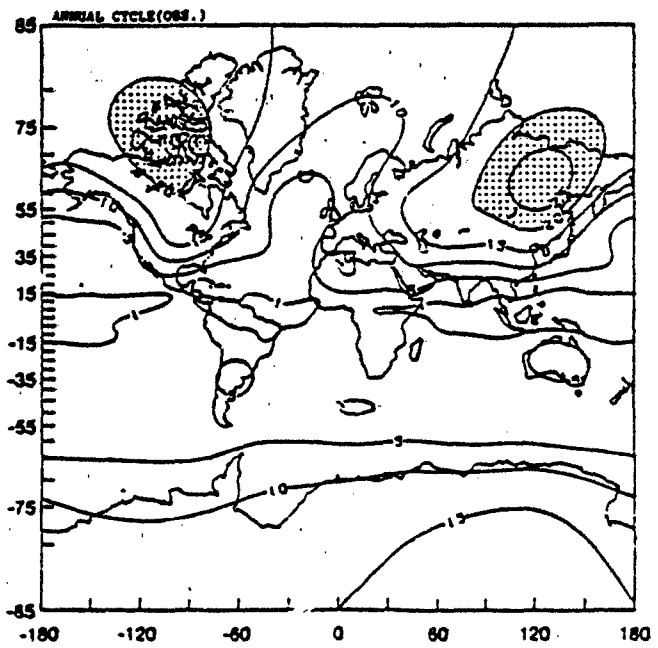
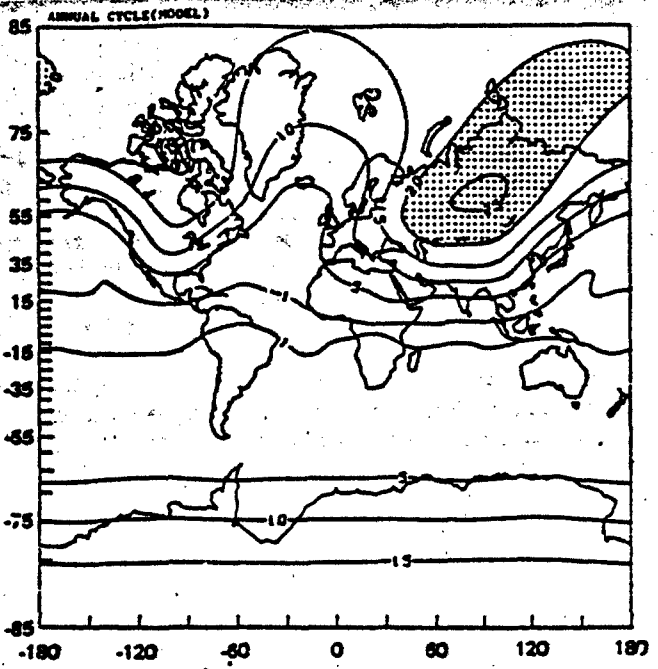


Figure 1. The amplitude (in $^{\circ}\text{C}$) of the normal seasonal cycle. The top panel shows results from the EBM; the bottom panel shows the observed cycle.

Figure 2 compares the seasonal phase lags, defined as the time between maximum solar heating and maximum temperature. Results within +15 degrees of the equator are not shown, because the amplitude of the cycle is small in this region; so the phase lags are poorly defined. Both the model and the observations show phase lags of the order of 30 days in continental areas, consistent with the cooling time scale discussed earlier. Over oceans, the maximum phase lag in the observations is roughly 75 days. The model tends to produce a nearly uniform phase lag of 90 days (one quarter cycle) over oceans. This corresponds to the lag of a linear system in the limit of infinite heat capacity. Considering the very small amplitude of the oceanic seasonal cycle (both in the observations and in the model), we do not view the discrepancy in the phase lags as a serious problem.

The second part of the validation procedure involved repeating soot experiments which had been run on GCMs. The GCM results were taken, in graphical form, from published reports. Because we did not have the GCM results available in digital format, it was not possible to perform the spatial filtering and replotting which would be desirable for direct comparison with the EBM results. A second aspect of these comparisons concerns the mode in which the EBM was run. For all soot experiments, the EBM used a land-sea distribution symmetrized about the prime meridian. Thus, a Western Hemisphere simulation actually refers to a globe with the western continents repeated at 180 degree intervals of longitude, and similarly for Eastern Hemisphere simulations. Experiments showed that this type of east-west symmetric model produced essentially the same results as an asymmetric model but with much less computing time since only the even-m modes of the spherical harmonics are used. The effect on the results is primarily cosmetic in that the eastern and western maps do not join smoothly at the boundary.

Covey, et al., (Reference 20) used the National Center for Atmospheric Research (NCAR) Community Climate Model (CCM) to simulate the effect of a fixed soot layer. The CCM solves the general circulation equations using spherical harmonics with an $L = 15$ cut-off. Vertical resolution is provided by a finite difference scheme with 9 levels. Sea surface temperatures are fixed, so no ocean response is permitted. The soot parameters assumed by Covey, et al., are:

- (1) purely absorbing at visible wavelengths,
- (2) optical depth = 3.0 at visible wavelengths,
- (3) latitude of soot band = 30° to 70°N , and
- (4) no effect on infrared radiation.

Figure 3 shows the surface temperature changes (with respect to control runs) for simulations starting on March 22 (top panel) and June 30 (bottom panel). In both cases, results are averaged over a 5-day period to smooth the meteorological "noise" of the model. The contours show intervals of 10°C in the surface temperature decrease.

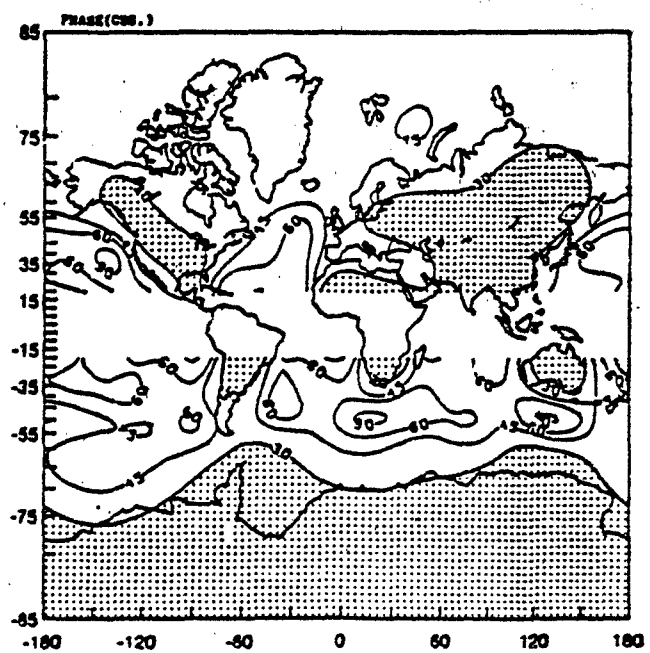
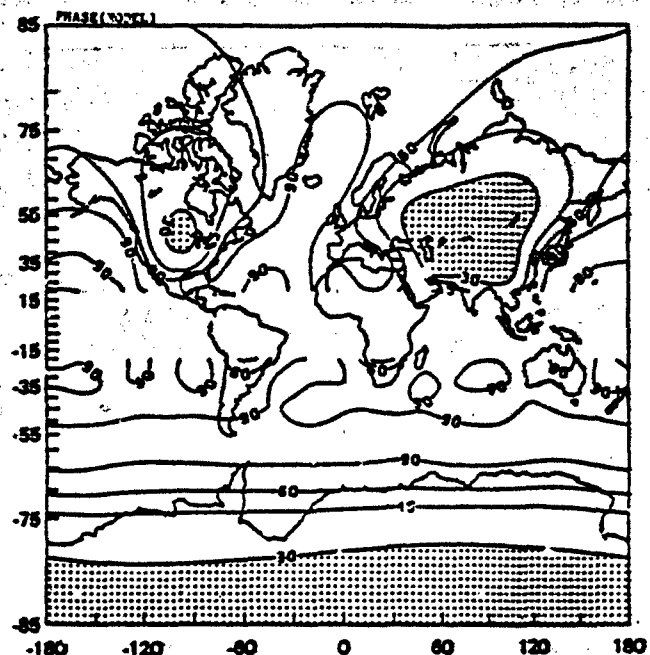


Figure 2. The phase lag (in days) of the normal seasonal cycle. Top panel shows FBM predictions; the bottom panel shows the observed cycle.

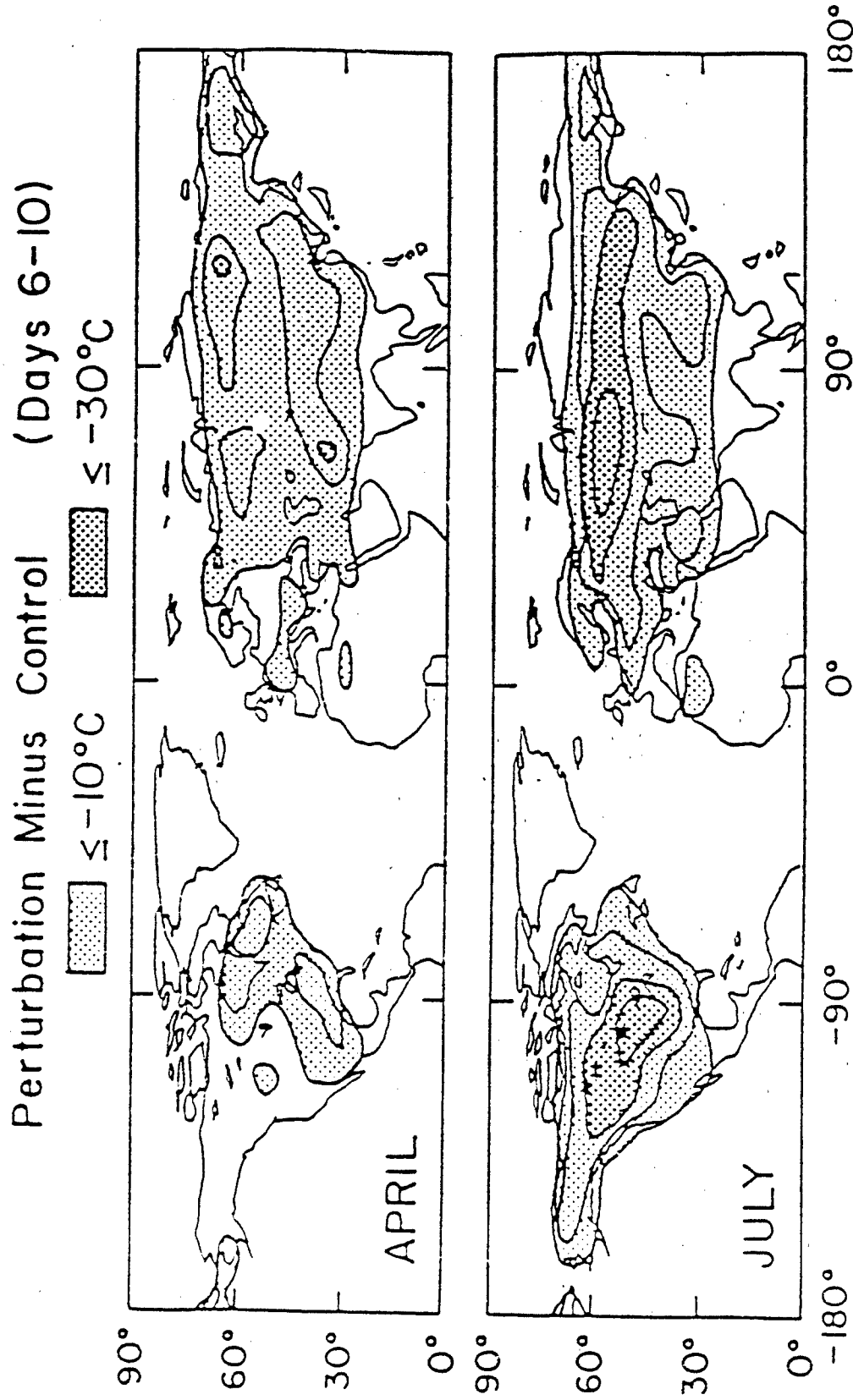


Figure 3. Temperature changes predicted by NCAR CGM, following injection of a uniform soot layer in a 30° to 70°N band.

For the same soot parameters, results obtained with the EBM are shown in Figure 4 (for spring conditions) and Figure 5 (for summer conditions). The soot effect was simulated by reducing the solar heating in the 30° to 70° N latitude band to 5 percent of the normal value for the season (that is, $\epsilon_{13} = 0.05$). Results are shown for day 10 of the simulations. Contours mark intervals of 2°C in the predicted temperature decrease.

In comparing these model predictions, the effect of the finer spatial resolution of the CCM is obvious. The temperature profiles in Figure 3 closely follow the continental boundaries. By comparison, these boundaries are blurred in the contours of Figures 4 and 5. Figure 3 also shows the effects of the large-scale circulation in the CCM. For instance, cooling tends to be less severe on the western sides of the continents than on the eastern sides. This is because, at mid-northern latitudes, the prevailing westerlies bring warm ocean air into the western regions of the continents. No such effect can occur in the EBM, which only allows for isotropic diffusion of heat.

Table 2 compares the maximum temperature decreases predicted by the two models. At each position in the table, the value from the CCM is given first, followed by the corresponding prediction of the EBM. This comparison shows that the EBM tends to underestimate the severity of the temperature decrease, as compared to the CCM. This may be attributed to two effects. First, as already noted in the discussion of the normal seasonal cycle, the response of the EBM to changes in solar heating tends to be too sluggish. Second, as a result of the coarser spatial resolution of the EBM, local temperature extremes are smoothed out over larger areas and decreased in amplitude. This comparison indicates that it would have been better to have included more spatial modes in the EBM solution.

Table 2. Maximum temperature changes for the NCAR scenario.

Season	CCM/EBM	
	Western Hemisphere	Eastern Hemisphere
Spring	$>20^{\circ}\text{C}/13^{\circ}\text{C}$	$>30^{\circ}\text{C}/24^{\circ}\text{C}$
Summer	$>40^{\circ}\text{C}/21^{\circ}\text{C}$	$>40^{\circ}\text{C}/35^{\circ}\text{C}$

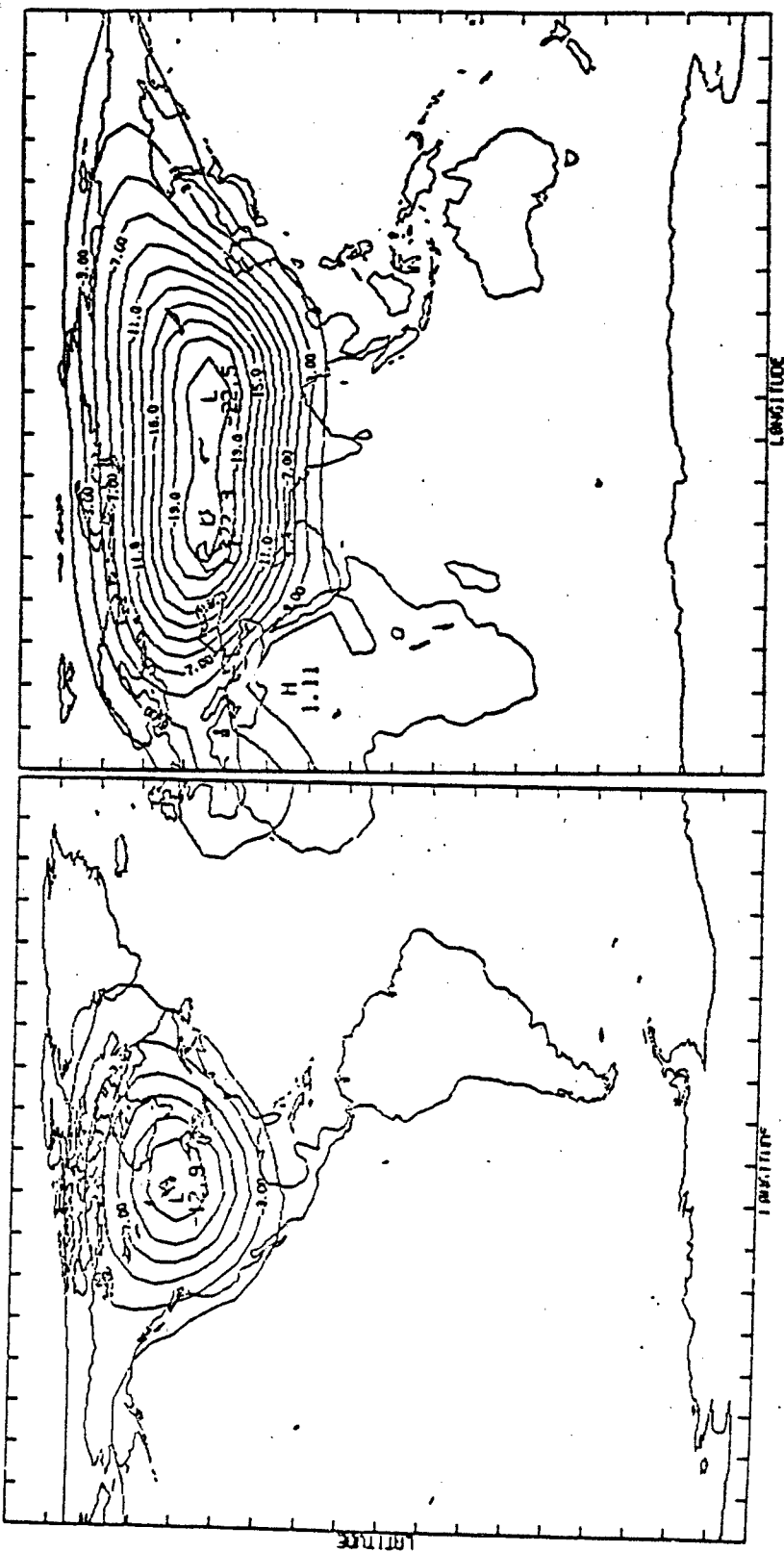


Figure 4. Temperature changes predicted by the EBM, following a springtime (22 March) injection of a uniform soot layer in a 30° to 70° N band.
Compare to top panel of Figure 3.

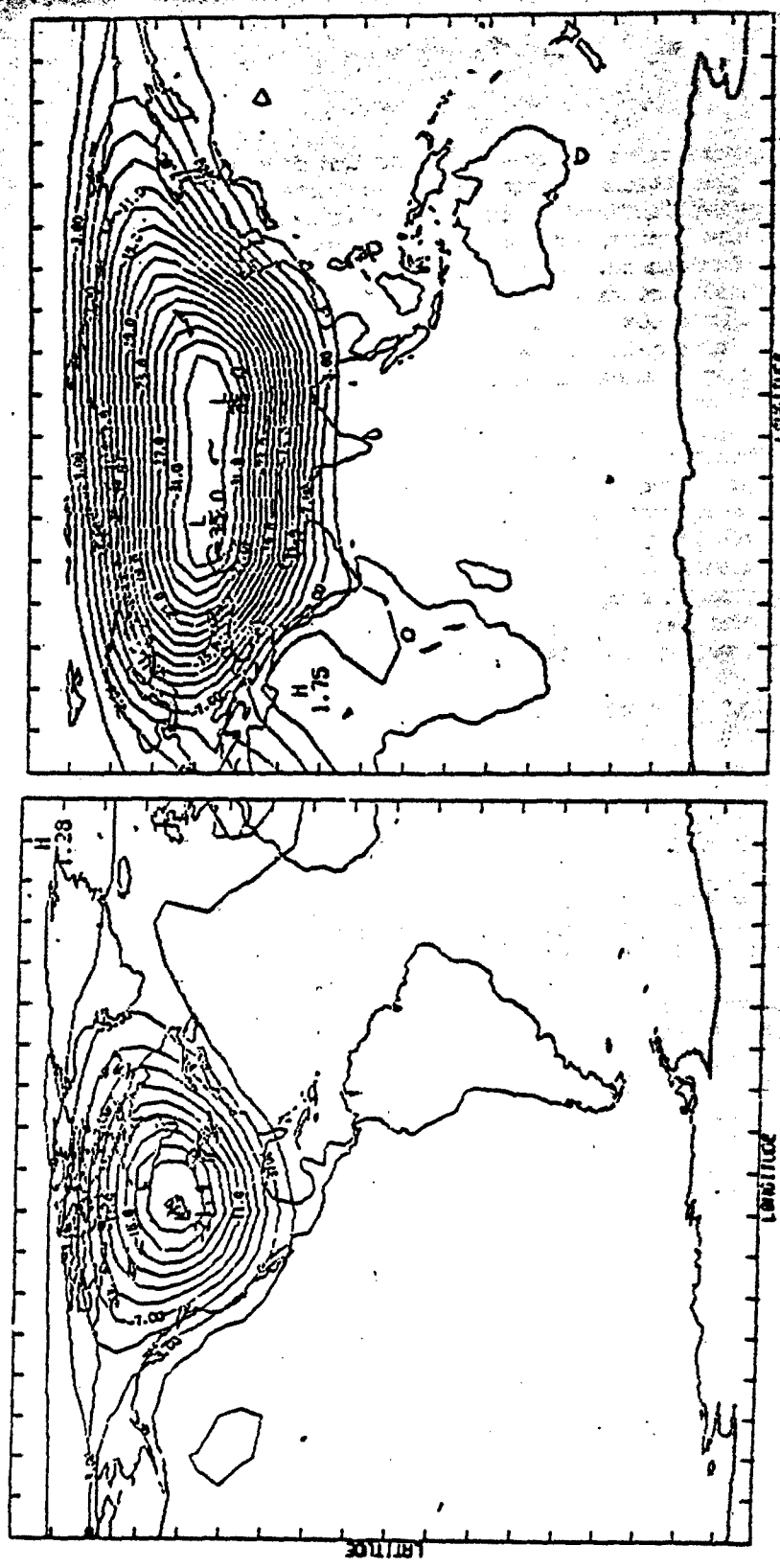


Figure 6. Temperature changes predicted by the EBM, following a summer (30 June) injection of a uniform soot layer in a 30° to 70° N band:
Compare to bottom panel of Figure 3.

In spite of these quantitative differences, the EBM does reproduce many features of the GCM predictions. Both models indicate that the largest temperature drops are confined to the deep continental interiors. In both cases, Table 2 shows that the cooling is more severe for summer runs and for the Eastern Hemisphere. We conclude that, although the EBM will not yield quantitatively accurate predictions, the major qualitative features are in agreement with GCM results. Given the present (and near-future) uncertainties in input data on the soot loading, it is doubtful that any type of global climate model is able to produce quantitatively accurate predictions.

Scientists at the Computer Center of the U.S.S.R. Academy of Sciences (CCAS) used a GCM to simulate the effects of a very dense soot layer, combined with a stratospheric dust layer (Reference 23). The CCAS model uses a horizontal grid with 12° latitude by 15° longitude resolution plus two vertical layers. Sea surface temperatures are allowed to vary in accordance with an energy balance equation for the ocean mixed layer. The model uses annual mean solar heating, so there is no seasonal cycle. The soot/dust parameters employed in the CCAS simulation are:

- (1) stratospheric dust layer reflects 70 percent of the incoming direct sunlight back to space,
- (2) tropospheric soot layer is purely absorbing with optical depth = 6.0 at visible wavelengths,
- (3) latitude of soot/dust = 12° to 90° N, and
- (4) no effect on infrared radiation.

Figure 6 shows the temperature changes, after 40 days, as computed by the CCAS model. Figure 7 shows the corresponding results obtained using the EBM, with the seasonal cycle turned off.

The geographical distributions of temperature changes shown in Figures 6 and 7 are very similar. In the Eastern Hemisphere, the major temperature changes extend much further south than in the NCAR scenario (Figures 3 to 5). For instance, large areas of Africa would experience temperature drops of more than 10°C , according both to the CCAS model and to the EBM. This occurs because the soot/dust layer now extends much further southward, where the solar heating is normally greatest. Quantitatively, the CCAS model and the EBM are in agreement with respect to the maximum temperature decrease for the Eastern Hemisphere. The CCAS simulation has a larger temperature drop in the Western Hemisphere than the EBM prediction (30°C vs. 23°C). This tendency of the EBM to underestimate Western Hemisphere temperature changes was also apparent in the comparison to the NCAR GCM.

A comparison of GCM results has been jointly published by the NCAR and CCAS groups (Reference 24). Although the two models show grossly similar results, the assumed soot/dust parameters and the simulated climates

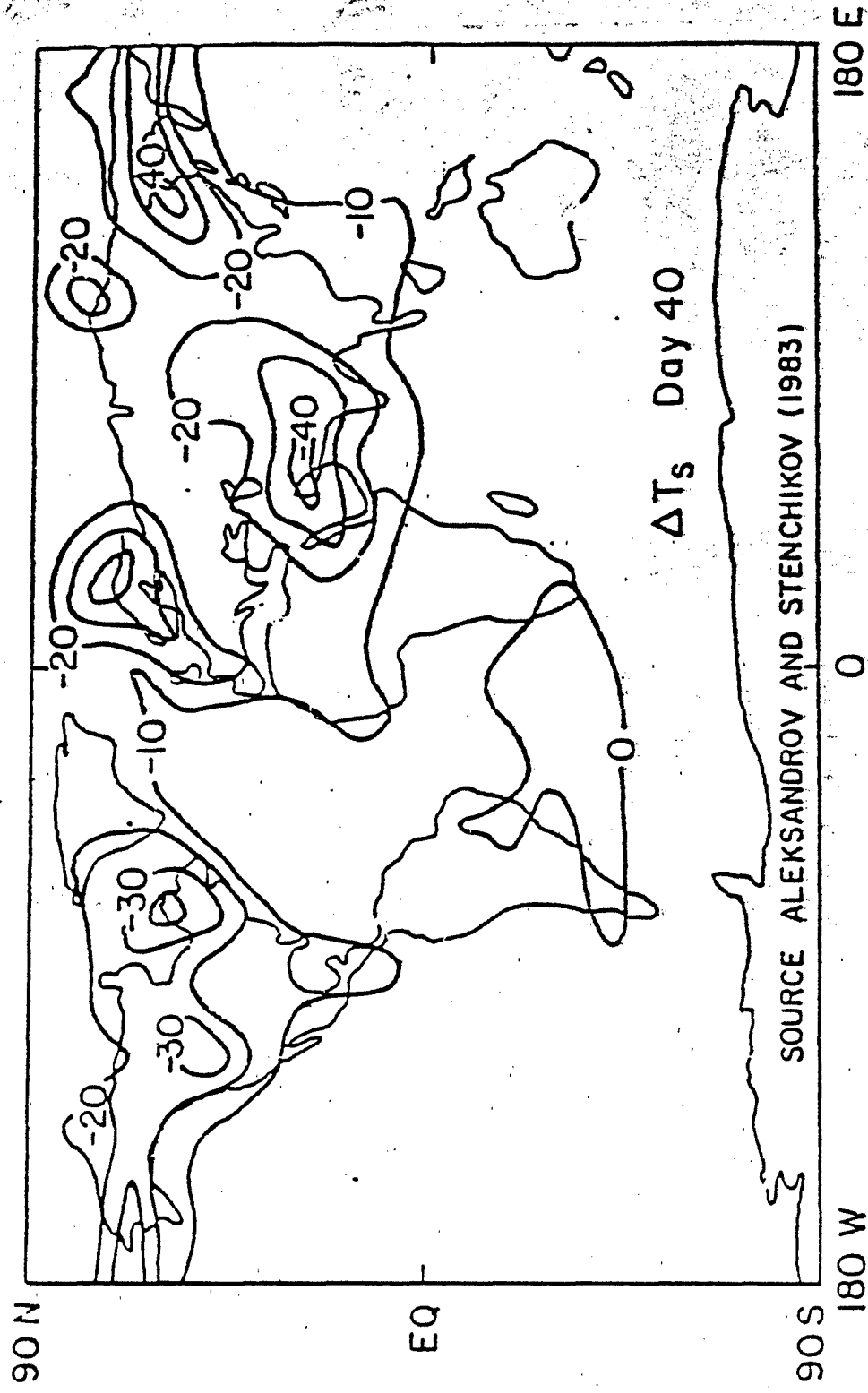


Figure 6. Temperature changes predicted by OGAS computer model (GCM plus ocean mixed layer), at 40 days after the initial soot/dust perturbation.

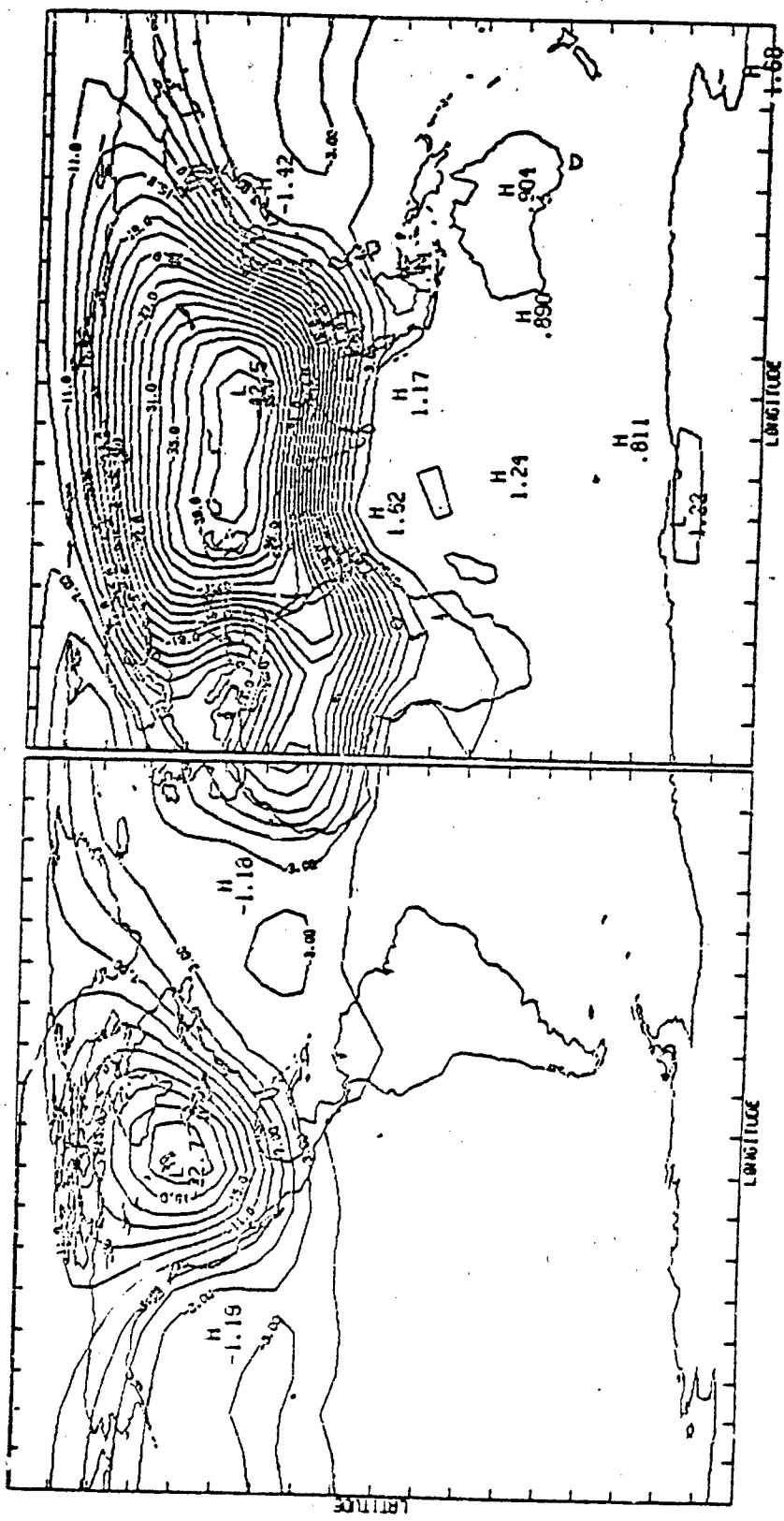


Figure 7. Temperature changes predicted by the EBM, at 40 days after perturbation, using the same soot/dust parameters as in the CCS simulation. Compare to Figure 6.

(seasonal vs. annual mean) are too different to allow any detailed comparisons. This points up an ambiguity in comparing EBM results to GCM results—the degree to which various GCMs would agree in their predictions for a given scenario is not known.

SENSITIVITY TO ASSUMED SOOT PARAMETERS

As remarked earlier, the major advantage of the EBM over more complex models is computational convenience. This allows for simulation of a wide variety of cases. Although the predicted climatic effects should not be considered quantitatively accurate, comparisons of results from different scenarios are useful in showing sensitivity to assumed parameters.

Baseline Case

The baseline case is derived largely from the 1985 study by the NAS (Reference 7). This scenario assumes a zonally uniform soot cloud confined between latitudes 30° to 70° N. The soot is purely absorbing to incoming sunlight and has no effect on outgoing infrared radiation. Initially, the cloud has an optical depth of 3.0 to sunlight. One-half of the soot is placed in the lower troposphere (below 5 km), where normal removal processes lead to a half-life of 3 days (e-folding time of 4.33 days). The remaining soot is placed in the 5 to 10 km layers, where the half-life for removal is 30 days (e-folding time of 43.3 days). Of course, in the one-level EBM, the only effect of the vertical distribution of soot is on the assumed removal rates. Symbolically, the removal rates are reflected in the time-dependence of the cloud optical depth at visible wavelength:

$$\tau_{\text{vis}}(t) = \tau_{\text{max}} \cdot (X_L e^{-t/4.33} + X_U e^{-t/43.3}) \quad (7)$$

where time is now measured in days since the initial soot injection and

$$\tau_{\text{max}} = 3.0, X_L = X_U = 1/2. \quad (8)$$

For the baseline case, the soot is assumed to be injected during the summer season (30 June).

Figure 8 shows Western Hemisphere maps of the induced surface temperature change (with respect to normal seasonal temperatures), at 10, 20, 40, and 80 days after the soot injection. The maximum effect occurs near day 20 of the simulation, when surface temperatures drop by as much as

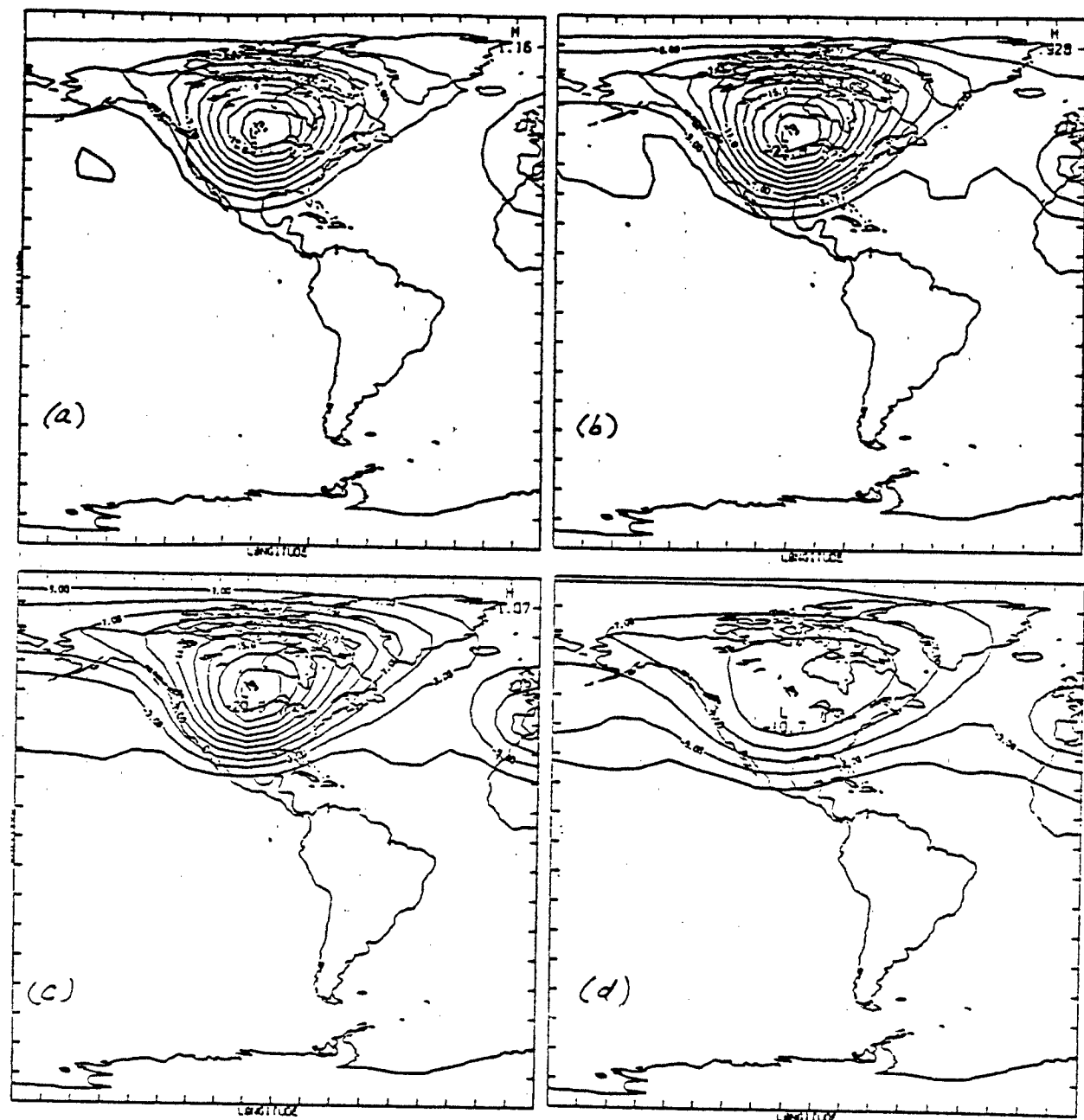


Figure 8. Temperature changes in the baseline/summer case at: (a) 10 days, (b) 20 days, (c) 40 days, and (d) 80 days.

23°C. (For sensitivity studies, it is sufficient to consider only the Western Hemisphere, since the other hemisphere behaves in a qualitatively similar manner.)

When considering the effects of a climatic anomaly on agriculture, the degree-day is a commonly used metric (Reference 25, Chapter 7). Here, we define degree-days as the difference between daily temperatures in the perturbed vs. control climates, summed over a specified length of time. Figure 9 displays a degree-day map for the baseline case, with the summation extending over a 1-year period after the initial soot injection. An interesting aspect of this map is that the degree-day contours do not follow coastlines nearly as closely as do the temperature contours. This is because, while the oceans cool more slowly than continental areas, the oceans also recover more slowly as the soot is removed. To a certain extent, this decreases the effect of the greater heat capacity of the oceans, in terms of a time-integrated quantity like degree-days. To the extent that biological damage depends on the duration, as well as severity of cooling, it appears that the consequences for marine biota are comparable to those in continental environments, particularly since marine life forms tend to be less tolerant to temperature changes (Reference 8).

The sensitivity tests involved various modifications of the baseline scenario. These modifications and the predicted effects are summarized in Table 3. The remainder of this section provides brief descriptions and comments on these simulations.

Seasonal Dependence

The cooling effect is obviously largest if soot injection takes place during the summer, since that is when the solar heating is normally greatest. With the exception of the NCAR/CCM simulation (Figure 3), little has been published regarding the consequences of soot injections in other seasons. As Table 3 shows, there is a strong seasonal dependence, both in the maximum cooling and in degree-days. Perhaps more surprising, the effects are very different for spring vs. autumn scenarios, particularly in the degree-day column. This is because the spring scenario occurs during the phase of the seasonal cycle when solar heating and surface temperatures are both normally increasing, in the Northern Hemisphere, at the maximum rate. The autumn scenario occurs when surface temperatures are normally decreasing, at a rate controlled, to a large extent, by the finite heat capacity rather than by solar energy effects.

Soot Removal Rates

The baseline case uses the assumed altitude distribution of the soot to estimate the removal rates, based on normal atmospheric cleansing processes. Cases 5 to 7 examine the dependence of the calculated climate

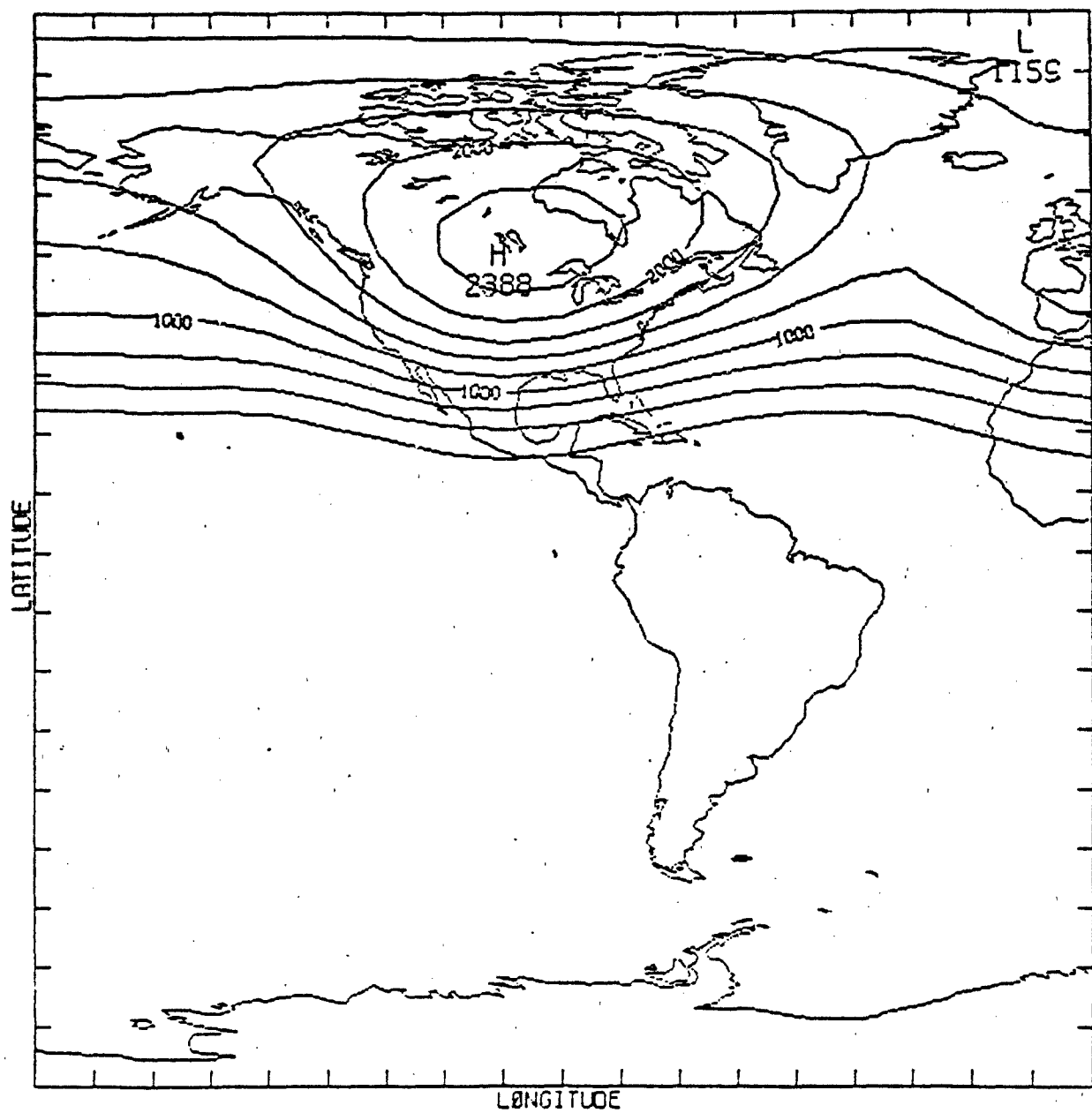


Figure 9. Degree-day map for the baseline/summer case, summed over a 1-year period following the initial smoke injection.

Table 3: Summary of Sensitivity Tests

Case #	Modification of Baseline	Max. Cooling (°C)	Degree -Days ^a
1.	Baseline/Summer	22.8	2388
2.	Baseline/Spring	17.0	2285
3.	Baseline/Winter	6.9	1092
4.	Baseline/Autumn	12.5	1188
5.	$X_L = 1, X_U = 0$	16.3	384
6.	$X_L = 2/3, X_U = 1/3$	19.6	1901
7.	$X_L = 0, X_U = 1$	28.8	3322
8.	Narrow latitude band	20.5	2147
9.	Two latitude bands	14.1	1733
10.	Outgoing infrared reduced 50%	14.0	1322

^a

Summed over one-year period after initial soot injection.

perturbation on the soot removal rate. In Case 5, the soot is assumed to occur only in the lower troposphere, where rapid removal occurs. The climatic perturbation is then less severe and of very short duration, as indicated by the factor of six reduction in degree-days. In Case 6, the soot is partitioned between the lower and upper troposphere in the ratio which represents a constant mixing ratio in the 0 to 10 km altitude range. In Case 7, all of the soot occurs in the upper troposphere, where the lifetime is very long.

A caution regarding interpretation of these results is in order. Since the EBM is a one-level model, it cannot treat the effects of the soot altitude distribution on radiative processes. Ramanathan and Kiehl (Reference 26) used a one-dimensional (vertical) radiative-convective model to examine atmospheric cooling rates for different soot altitude profiles. They found that the surface cooling rate is cut in half if a constant mixing ratio with a scale height of 3 km is assumed. This occurs because much of the solar radiation is absorbed near the planetary boundary layer which interacts strongly with the surface. Such effects are neglected in the EBM. Furthermore, the assumption of a fixed height distribution (modified only by removal) is very artificial. In reality, the radiatively heated soot cloud will tend to rise over an extended period of time, as discussed in Section 3.

Horizontal Soot Distribution

In the first few days after a nuclear war, the soot would be confined to isolated clouds or plumes, over the fire sites. If the soot remains in the atmosphere for several days, normal circulation plus winds created by horizontal thermal gradients would tend to move the soot away from the fire sites. The geographical distribution of the soot cloud would then depend on the distribution of fire sites, on normal circulation patterns, and on the anomalous circulations created by locally uneven heating and cooling. It is by no means obvious that the result of transport would be a cloud layer which is approximately uniform in a broad latitude band.

Because climate models are barely able to resolve the synoptic scale, climate simulations have assumed that the soot cloud is uniform between specified boundaries. The simplest case (disregarding the totally unrealistic case of a global cloud) is a zonally uniform cloud between specified northern latitudes. This assumption may be partially justified by the similar latitudes of the primary target areas in both the Eastern and Western Hemispheres, and by the highly zonal character of normal circulation patterns at the target latitudes. For instance, the baseline case assumes that the soot lies in a band between latitudes 30° to 70°N, as did the NCAR study (Reference 20).

To test the sensitivity of the simulated climate to this assumption, Cases 8 and 9 used zonal cloud bands with different boundaries. For Case 8, the cloud band was confined between 40° and 60°N . Since this represents only one-half the cloud extent in the baseline case, the optical depth was doubled (i.e., $\tau_{\text{MAX}} = 6.0$) so that the assumed total soot mass was the same in both cases. As indicated in Table 3, this results in a very slight reduction in the severity of the climate effect. Note that, in Case 8, the optical depth under the cloud is, at any given time, twice as large as in the baseline case. As a result, the optical depth is greater than unity for 48 days in Case 8, as opposed to 18 days in the baseline case. This longer duration is, however, completely compensated by the fact that the center of the cloud band is now much closer to the unshaded latitudes, so horizontal diffusion of heat from these latitudes is more important.

Case 9 takes a different approach to the issue of soot cloud location. The soot was confined to two bands, between 20° to 40°N and between 60° and 80°N . The solar heating in the gap (40° to 60°N) was left at normal values to simulate the effect of a broken cloud layer. The maximum temperature effect for this case is 40 percent smaller than for the baseline case, while the degree-day effect is reduced by 30 percent (see Table 3).

The geographical distribution of the climate anomaly for this case is very significant. Figure 10 shows a temperature difference map (Case 9 minus control) on day 30, which corresponds to the greatest cooling; the degree-day distribution, summed over 1 year, is shown in Figure 11. Note that, in both figures, the greatest excursions occur in the band covered by the more northern soot cloud. This is surprising in that the larger absolute reduction in solar heating occurs in the more southern soot band, where the normal solar flux is larger. As in Case 8, horizontal transport of heat plays a very important role in these simulations with narrow cloud bands. The southern soot band is heated on both sides by horizontal heat transport from unshaded latitudes. The northern soot band extends nearly to the pole. As a result, the unshaded region northward of this band is small in area and receives little solar energy, so the region in the soot band can only be heated by horizontal transport from the unshaded area to the south. This simulation points out the importance of heat transport from clear areas into soot regions when the soot cloud is limited in extent. For reasons given above, the southern soot band may be more representative of this effect. In this region, the maximum temperature decrease is only $\sim 10^{\circ}\text{C}$, i.e., less than one-half of the temperature decrease in the baseline case.

As argued earlier, there are no compelling reasons to expect that the soot cloud would expand into a broad and uniform zonal band. Tracer calculations, using normal atmospheric circulation as input, indicate that the soot cloud will spread out from the target areas, but this spreading would be far from uniform (Reference 27). This calculation probably

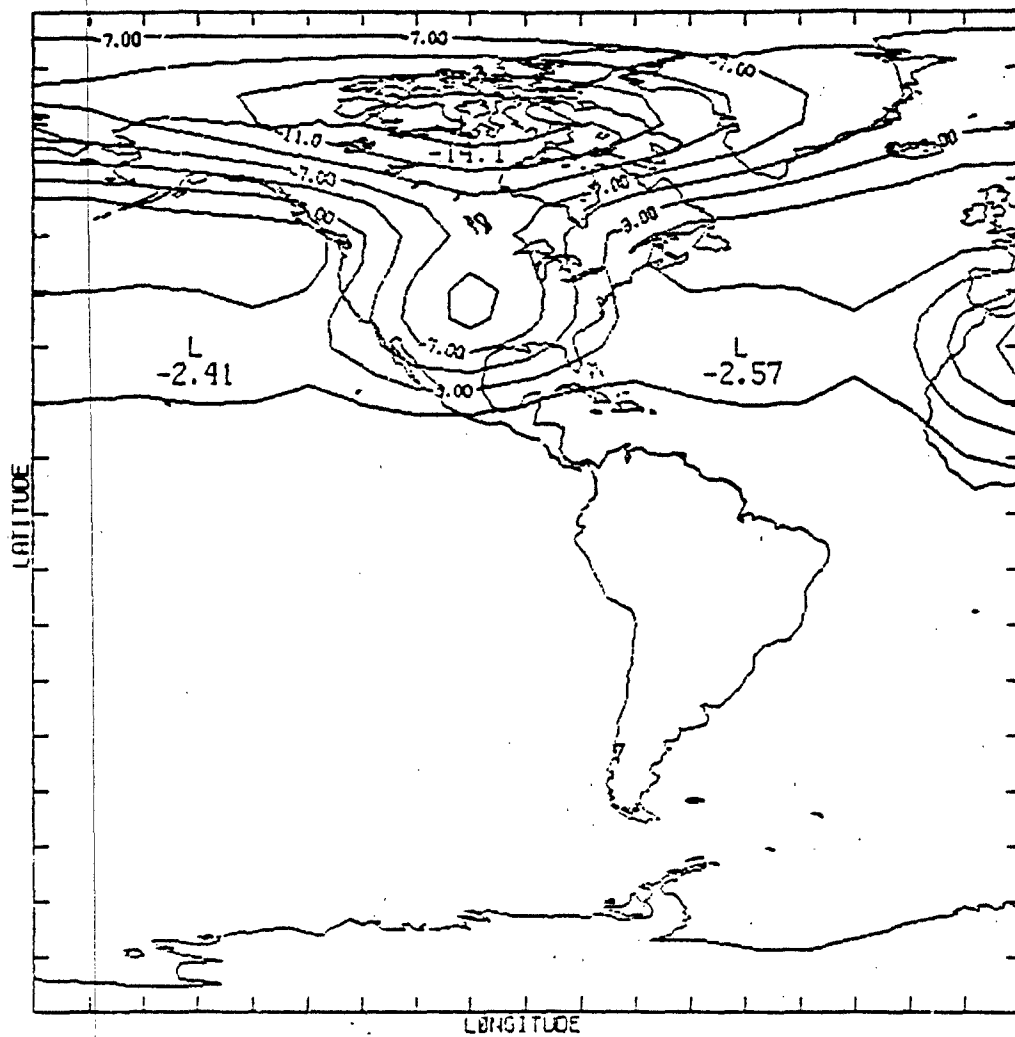


Figure 10. Temperature differences (perturbed minus control) at day 30 in the Case 9 simulation.

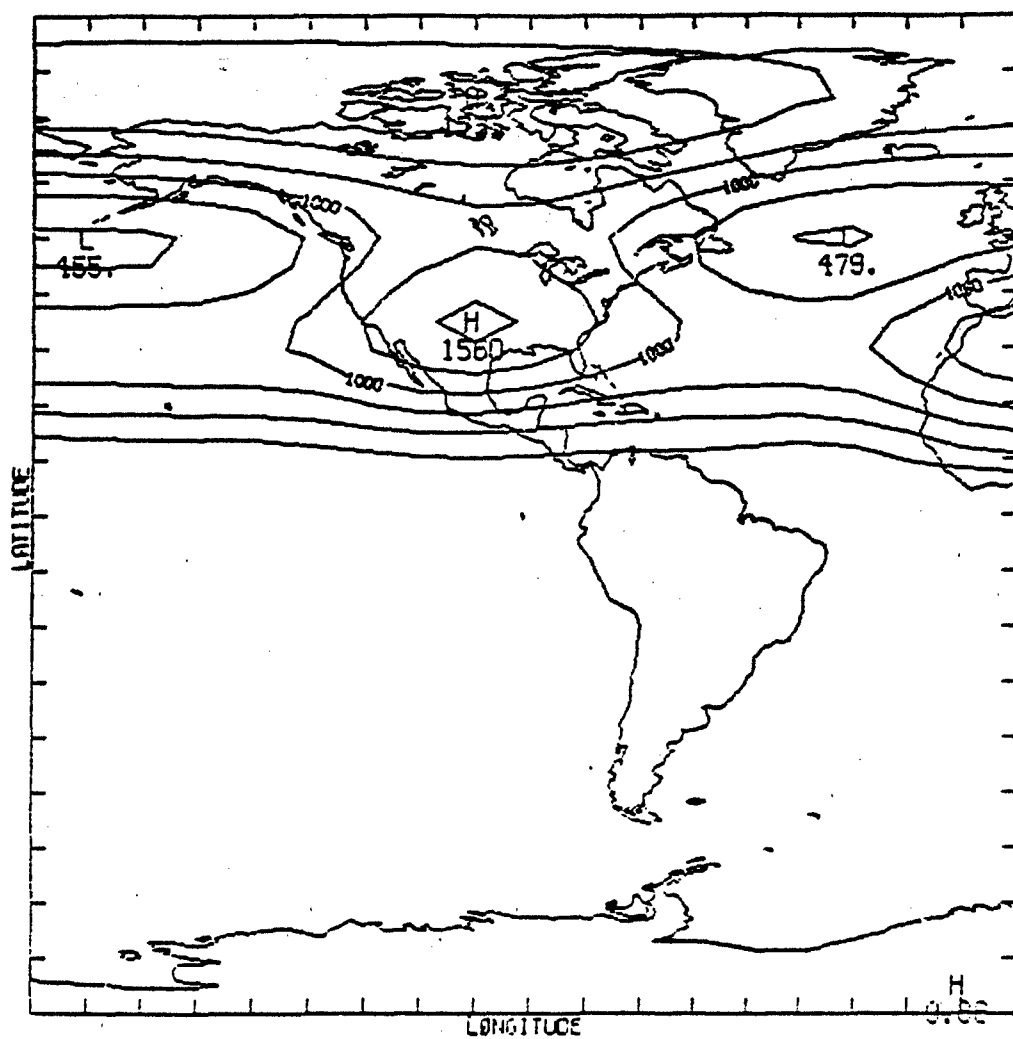


Figure 11. Degree-day map for the Case 9 simulation, summed over a 1-year period following the initial smoke injection.

overestimates the degree of uniformity, due to limited spatial resolution of the input winds and due to numerical diffusion in the transport algorithm.

It would be of interest to simulate the effect of narrower soot bands than considered in Cases 8 and 9, as well as soot clouds having longitudinal variations, in addition to latitudinal structure. Longitudinal variations would allow heat transport to occur in both of the horizontal dimensions. This was not possible with the current version of the EBM because: (a) the limited number of modes retained in the spherical harmonic expansion [Equations (4) to (6)] sets the resolution at about 15° of latitude; and (b) the current implementation of the EBM assumes a zonally uniform soot cloud. However, neither of these limitations are inherent in the basic model, so these issues could be examined in future investigations.

Outgoing Infrared Radiation

The climate simulations assume that the soot cloud is transparent to infrared radiation. This is a critical assumption since absorption of incoming sunlight, coupled with the transparency to outgoing thermal energy, leads directly to the predicted cooling. While it is true that submicron particles of pure soot absorb mainly at visible (or shorter) wavelengths, the actual cloud resulting from fires would not consist of pure soot. Large amounts of water vapor, carbon monoxide, and nitrogen oxides would be entrained in the fire plumes, along with a vast inventory of hydrocarbons and toxic chemicals produced by incomplete combustion (Reference 28). Many of these gases are strong absorbers in the infrared.

To test the effect of increased infrared opacity, we reduced the outgoing infrared fluxes in the EBM, within the soot band. The maximum reduction was 50 percent, with a return to normal fluxes as the soot was removed. As expected, the severity of the climate modification was significantly reduced (see Table 3). Unfortunately, a realistic estimate of the infrared opacity will require detailed consideration of atmospheric chemistry, which is beyond the scope of this report. The results of Case 10 show that the Nuclear Winter problem is sensitive to infrared opacity, but the predictions must not be interpreted as a quantitative estimate.

SECTION 3

RECOMMENDATIONS

The EBM simulations described in Section 2 demonstrate the applicability of this type of model to the soot-cooling problem. While the results should not be interpreted as quantitative predictions, they are useful in delineating sensitivity of the predicted climate modification to uncertainties in the input parameters. The more complex GCMs share these uncertainties in that radiation, scavenging processes, tropospheric chemistry, and sub-grid-scale transport are either heavily parameterized or totally ignored. Such models are too cumbersome to allow the type of sensitivity testing described in Section 2. Thus, the flexibility of the EBM to simulate many cases complements the more powerful predictive capabilities of the GCMs.

The important new implication to be drawn from the sensitivity tests is that the severity of the climate modification depends critically on the lateral extent and uniformity of the soot cloud. If the cloud is broken or confined to narrow strips, heat from nearby unclouded regions will be transported into the clouded areas, thereby limiting the surface temperature decrease. There has been speculation that a very nonuniform soot layer would have a reduced climatic impact because the soot particles would be less effective in absorbing sunlight (i.e., optical depths would vary between very large and very small values). While this reasoning is correct, Case 9 shows that the climatic impact is reduced even if the broken soot cloud is distributed such that the total sunlight absorbed is equal to that absorbed in the baseline case (i.e. a broad and uniform cloud).

This case points to the importance of properly accounting for the lateral transport and spreading of the soot cloud away from localized fire sites. While the basic physics of atmospheric transport is well understood, the ability to model this process is limited because such modeling requires both high resolution (down to the plume scale) and large domain (up to the planetary scale). GCMs will definitely not be able to properly handle this problem, so appropriate parameterizations of sub-grid-scale soot-cloud structure will have to be developed. Simpler models, such as the EBM, can be useful in developing and testing various schemes for simulating the effects of nonuniform or broken soot clouds.

The EBM was also used to demonstrate sensitivity of the climate effect to: the assumed season, the soot removal rate, and the effect of the atmospheric loading on infrared radiation. In these cases, the model results confirm intuitive expectations that the severity of the climate modification is very dependent on these factors.

As a final note, we offer a warning regarding interpretation of model predictions for the climate modification scenario. When dealing with very complex models, such as GCMs, it is tempting to accept the predictions without scrutinizing whether the basic processes are properly handled by the models; the tremendous amount of detail in the models can give a false sense of security. An example will be provided to illustrate this danger, based on the recent GCM simulation, carried out at Los Alamos (Reference 29). This simulation represents the current state-of-the-art in global effects modeling.

SELF-LOFTING OF THE SOOT LAYER

The major improvement of the Los Alamos simulation over other models is that the soot is interactive (i.e., directly participates in the energy balance and dynamics of the simulated atmosphere). The most significant new feature to emerge from the Los Alamos simulation is that, because the soot absorbs sunlight, it heats and rises into the stratosphere. This self-lofting is critically important because the lifetime of the soot is much longer once the soot rises above the precipitating layers of the atmosphere.

There is little question that there is a potential for self-lofting if the soot layer survives initial scavenging. However, it is doubtful that a GCM can directly follow this process. Figure 12 provides a schematic illustration of how the lofting process will likely proceed. The top panel shows an initial configuration consisting of a horizontally uniform soot layer. Since the optical depth is greater than unity, much of the soot is shielded from direct sunlight. The middle panel shows a perturbation of the uniform cloud, consisting of a local upward intrusion. Such a perturbation could, for instance, be created by local convective processes. This intrusion will be heated more rapidly than the remaining soot layer because it provides a larger surface area for intercepting sunlight. As a result, the intrusion will rise faster than the uniform layer, as illustrated in the bottom panel.

This instability of the uniform soot layer is an example of multi-component (or "double-diffusive") convection (Reference 30). Such processes have been widely studied in the laboratory and in oceanography, where the intrusions are referred to as "salt fingers". Figure 13 shows a laboratory example of upward-propagating, double-diffusive convection.

In contrast to this highly structured physical process, GCMs are restricted to the very uniform cloud layer shown in the top panel of Figure 12. The Los Alamos GCM, which is based on the NCAR/CCM, has horizontal resolution of roughly 500 km and vertical resolution of the order of 1 km

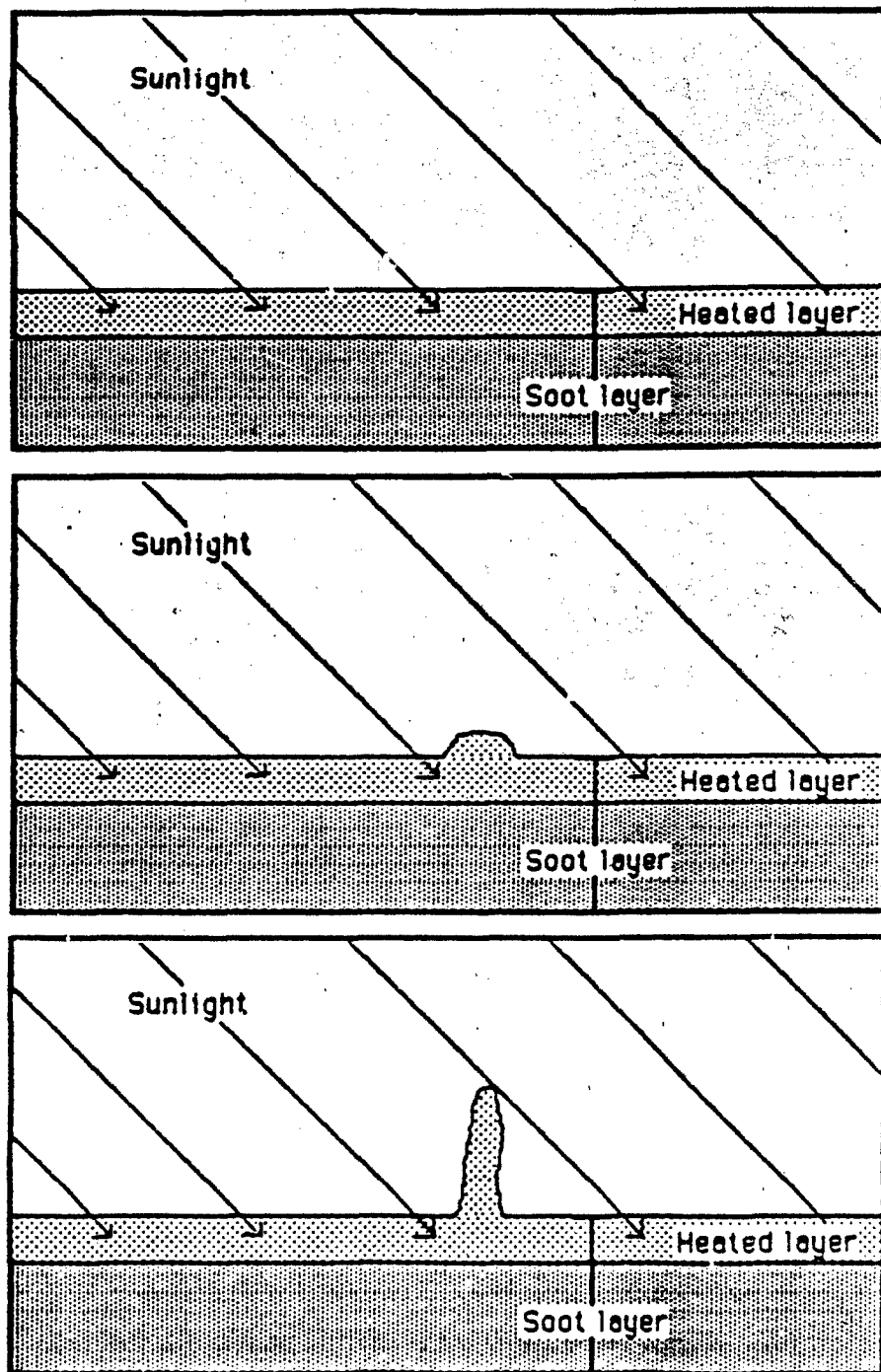


Figure 12. Development of a double-diffusive instability in a uniform soot cloud. Top panel: initial conditions, consisting of a horizontally uniform, optically thick cloud. Middle panel: perturbation of the initial condition. Bottom panel: growth of the perturbation due to enhanced solar heating.

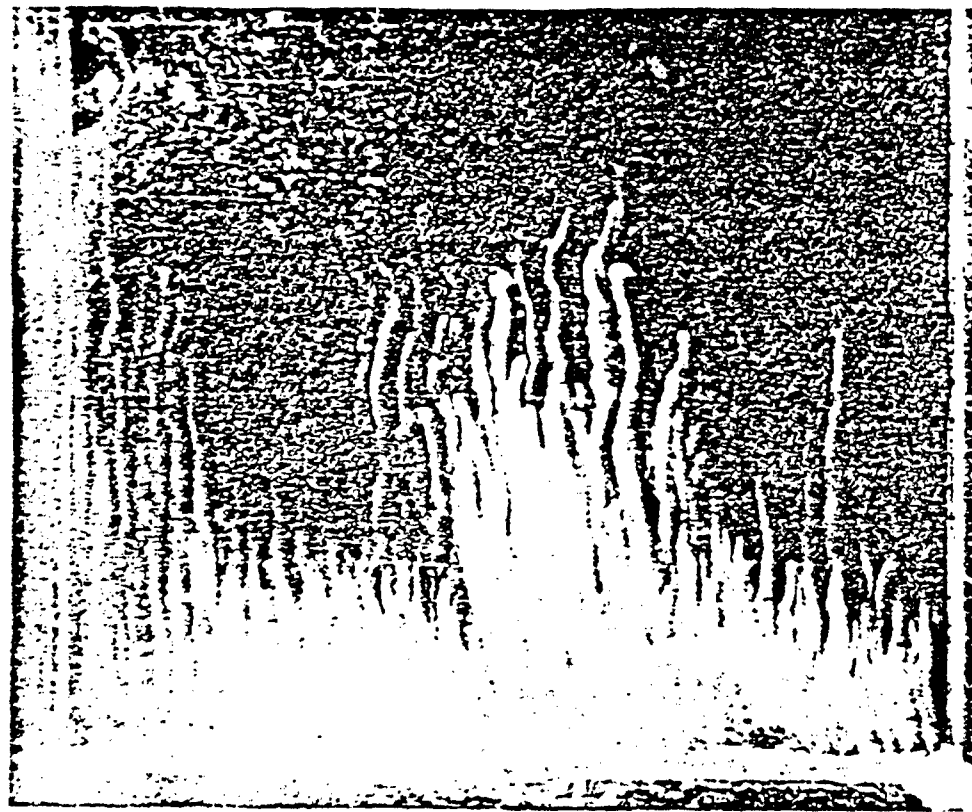


Figure 13. A laboratory example of double-diffusive convection produced by placing hot salty water over cool fresh water. The fresh water is marked by fluorescent dye. From Reference 30.

at the cloud level. In other words, the basic model cell is a very thin plate (aspect ratio of 50:1). Such a model cannot directly follow the self-lofting process, which will have a horizontal/vertical aspect ratio $\ll 1$ (as in Figure 13). In fact, the double-diffusive instability makes it unlikely that a broad and horizontally uniform cloud will ever form.

SECTION 4

LIST OF REFERENCES

1. National Research Council. "Long-Term Worldwide Effects of Multiple Nuclear Weapons Detonations." National Academy of Sciences, Washington, DC, 1975.
2. Knox, J. B.. "Global Scale Deposition of Radioactivity from a Large-Scale Exchange." Report UCRL-88907, Lawrence Livermore Laboratory, 1983.
3. Foley, H. M., and Ruderman, M. A., "Stratospheric NO Production from Post-Nuclear Explosions." Journal of Geophysical Research, 78, p. 4441, 1973.
4. Luther, F. M., "Nuclear War: Short-Term Chemical and Radiative Effects of Stratospheric Injections." Report UCRL-89957, Lawrence Livermore National Laboratory, 1983.
5. Crutzen, P. J., and Birks, J. W., "The Atmosphere After a Nuclear War: Twilight at Noon." Ambio, 11, p. 115, 1982.
6. Turco, R. P., Toon, O. B., Ackerman, T. P., Pollack, J. B., and Sagan, C., "Nuclear Winter: Global Consequences of Multiple Nuclear Explosions." Science, 222, p. 1283, 1983.
7. National Research Council. "The Effects on the Atmosphere of a Major Nuclear Exchange." National Academy of Sciences, Washington, DC, 1985.
8. Ehrlich, P. R., et al., "Long-Term Biological Consequences of Nuclear War." Science, 222, p. 1293, 1983.
9. Gates, W. L.. "Modeling in the Ice-Age Climate." Science, 191, p. 1138, 1976.
10. Manabe, S., and Hahn, D. G., "Simulation of the Tropical Climate of an Ice Age." Journal of Geophysical Research, 82, p. 3889, 1977.
11. Budyko, M. I.. "The Effect of Solar Radiation Variations on the Climate of the Earth." Tellus, 21, p. 611, 1969.
12. Sellers, W. D., "The Effect of Changes in the Earth's Obliquity on the Distribution of Mean Annual Sea-Level Temperatures." Journal of Applied Meteorology, 9, p. 960, 1970.

13. North, G. R., Cahalan, R. F., and Coakley, J. A., "Energy Balance Climate Models," Reviews of Geophysics and Space Physics, 19, p. 91, 1981.
14. Robock, A., "Snow and Ice Feedbacks Prolong Effects of Nuclear Winter," Nature, 310, p. 667, 1984.
15. North, G. R., Mangel, J. G., and Short, D. A., "Simple Energy Balance Model Resolving the Seasons and the Continents: Application to the Astronomical Theory of the Ice Ages," Journal of Geophysical Research, 88, p. 6576, 1983.
16. Hays, J. D., Inbrie, J., and Shackleton, N. J., "Variations in the Earth's Orbit: Pacemaker of the Ice-Ages," Science, 194, p. 1121, 1976.
17. Wilson, R. C., Gulkis, S., Janssen, M., Hudson, H. S., and Chapman, G. A., "Observations of Solar Irradiance Variations," Science, 211, p. 700, 1981.
18. Stephens, G. L., Campbell, G. G., and Vonder Haar, T. H., "Earth Radiation Budgets," Journal of Geophysical Research, 86, p. 9739, 1981.
19. North, G. R., and Coakley, J. A., "Differences Between Seasonal and Mean Annual Energy Balance Model Calculations of Climate and Climate Sensitivity," Journal of the Atmospheric Sciences, 36, p. 1189, 1979.
20. Covey, C., Schneider, S. H., and Thompson, S. L., "Global Atmospheric Effects of Massive Smoke Injections from a Nuclear War: Results from General Circulation Model Simulations," Nature, 308, p. 21, 1984.
21. Crutcher, H. L., and Maserve, J. M., "Selected Level Heights, Temperatures and Dew Points for the Northern Hemisphere," Report NAVAIR 50-1C-52 (revised), Chief of Naval Operations, Washington, DC, 1970.
22. Taljaard, J. J., Van Loon, H., Crutcher, H. L., and Jenne, R. L., "Climate of the Upper Air: Southern Hemisphere, I. Temperatures, Dew Points, and Heights at Selected Pressure Levels," Report NAVAIR 50-1C-55, Chief of Naval Operations, Washington, DC, 1969.
23. Alekseev, V. V., and Stenchikov, G. L., "On the Modeling of the Climatic Consequences of Nuclear War," The Proceedings on Applied Mathematics, Computing Center of the USSR Academy of Sciences, 1983.

24. Thompson, S. L., Aleksandrov, V. V., Stenchikov, G. L., Schneider, S. H., Covey, C., and Chervin, R. M., "Global Climatic Consequences of Nuclear War: Simulations with Three-Dimensional Models," Ambio, in press, 1984.
25. Ahrens, D. C., "Meteorology Today," West Publishing Co., St. Paul, Minnesota, 1982.
26. Ramanam, V., and Kiehl, J. T., "Sensitivities of the Radiative Forcing Due to Large Loadings of Smoke and Dust Aerosols," Journal of Geophysical Research, submitted, 1985.
27. MacCracken, M. C., and Walton, J. J., "The Effects of Interactive Transport and Scavenging of Smoke on the Calculated Temperature Change Resulting from Large Amounts of Smoke," Proceedings of the International Seminar on Nuclear War, Erice, Italy, in press, 1985.
28. Birks, J. W., and Staehelin, J., "Changes in Tropospheric Composition and Chemistry Resulting from a Nuclear War," preprint, 1985.
29. Malone, R., Auer, L., Glatzeder, G., Wood, M., and Toon, B., "Interactive Aerosol Transport and Scavenging Studies with a GCM," Global Effects Program Meeting, Santa Barbara, 12-14 February, 1985.
30. Turner, J. S., "Double-Diffusive Phenomena," Annual Review of Fluid Mechanics, 6, p. 37, 1974.

APPENDIX

MATHEMATICAL PROPERTIES OF THE CLIMATE MODEL

The climate model defined by Equation (1) has both time- and space-dependence. The mathematical properties of this model concern the e-folding time for response to a time-dependent perturbation, and the characteristic length for propagation of a localized perturbation. In principle, these properties could be derived by applying a formal Green's function analysis. However, this is unnecessarily complex; we take a less rigorous approach based on examination of the specific terms governing time- and space-propagation of a perturbation.

To derive the e-folding time, we consider a spatially averaged version of Equation (1). The diffusion term then vanishes, leaving

$$C \frac{dT(t)}{dt} = QoS(t) - [A + BT(t)]. \quad (\text{A.1})$$

We consider $S(t)$ to be the source term for driving a step-function perturbation of this equation:

$$S(t) = \begin{cases} S_0 & \text{for } t \leq 0 \\ S_1 & \text{for } t > 0 \end{cases} \quad (\text{A.2})$$

Assuming that the model is in equilibrium for $t \leq 0$, at a temperature

$$T_0 = (QoS_0 - A)/B. \quad (\text{A.3})$$

the solution to Equation (A.1) for $t > 0$ is

$$T(t) = T_1 + (T_0 - T_1)e^{-Bt/C} \quad (\text{A.4})$$

where

$$T_1 = (QoS_1 - A)/B \quad (\text{A.5})$$

From Equation (A.4), we see that $T(t) \rightarrow T_1$, as $t \rightarrow \infty$, and that the e-folding time for the temperature response is

$$\tau = C/B \quad (\text{A.6})$$

To derive the characteristic length scale, we rewrite Equation (1) in the form

$$\frac{1}{T} \frac{\partial T}{\partial t} - \frac{B}{C} \frac{Q_{AS} - A}{BT} = \frac{D}{C} \frac{\nabla^2 T}{T} - 1 \quad (A.7)$$

where time- and space-dependence of the appropriate variables is still implied. Examining this equation, it is apparent that the left side is the inverse of the e-folding time for temperature. The first term on the right side involves only radiation quantities (solar and infrared), while the second term represents horizontal energy transport. The temperature time scale is thus the harmonic sum of the radiation and transport time scales:

$$\frac{1}{T_{\text{temperature}}} = \frac{1}{T_{\text{radiation}}} + \frac{1}{T_{\text{transport}}} \quad (A.8)$$

where the time scales are evaluated by term-by-term comparison of Equations (A.7) and (A.8). We now consider the consequences of a localized perturbation in temperature. Due to the diffusion term, the perturbation will propagate outward at a rate set by $T_{\text{transport}}$. As it propagates, it will be damped by radiative processes, at a rate set by $T_{\text{radiation}}$. A characteristic distance to which the disturbance will propagate is obtained by

$$T_{\text{transport}} = T_{\text{radiation}} \quad (A.9)$$

or

$$\frac{D}{C} \frac{1}{T} = \frac{B}{C} \frac{Q_{AS} - A}{BT} = - \left(\frac{B}{C} \frac{Q_{AS} - A}{BT} - 1 \right) \quad (A.10)$$

The characteristic length, ℓ , of the diffusion operator is given by

$$\frac{1}{\ell^2} = \frac{1}{T} \frac{B}{D} \frac{Q_{AS} - A}{BT} = - \left(\frac{B}{C} \frac{Q_{AS} - A}{BT} - 1 \right) \quad (A.11)$$

Finally, since the equilibrium temperature is given by

$$T_{\text{eq}} = \frac{Q_{AS} - A}{B} \quad (A.12)$$

Equation (A.11) becomes

$$\frac{1}{l^2} = - \left(\frac{B}{D} \frac{T_{eq}}{T} - 1 \right) \quad (A.13)$$

and the characteristic length scale is of order

$$l = \sqrt{D/B} \quad (A.14)$$

DISTRIBUTION LIST

DEPARTMENT OF DEFENSE

ASSISTANT SECRETARY OF DEFENSE
CMD, CONTROL, COMMUNICATIONS & INTEL
ATTN: DASD(CI)

ASSISTANT TO THE SECRETARY OF DEFENSE
ATTN: EXECUTIVE ASSISTANT

DEF RSCH & ENGRG
ATTN: STRAT & SPACE SYS(OS)

DEFENSE ADVANCED RSCH PROJ AGENCY
ATTN: GSD R ALEWINE
ATTN: T TETHER

DEFENSE COMMUNICATIONS AGENCY
ATTN: A200 R CRAWFORD
ATTN: A320 P BIRD
ATTN: A730 G JONES
ATTN: J KAPLAN

DEFENSE COMMUNICATIONS ENGINEER CENTER
ATTN: CODE R123 (TECH LIB)

DEFENSE INTELLIGENCE AGENCY
ATTN: DIR
ATTN: DT-1B
ATTN: RTS-2B

DEFENSE NUCLEAR AGENCY
ATTN: OPNA
3 CYS ATTN: RAAE
ATTN: RAAE K SCHWARTZ
ATTN: RAAE P LUNN
4 CYS ATTN: TITL

DEFENSE TECHNICAL INFORMATION CENTER
12 CYS ATTN: DO

FIELD COMMAND DEFENSE NUCLEAR AGENCY
ATTN: FCTXE

FIELD COMMAND DNA DET 2
LAWRENCE LIVERMORE NATIONAL LAB
ATTN: FC-1

JOINT CHIEFS OF STAFF
ATTN: C3S
ATTN: C3S EVALUATION OFFICE (HQDOO)
ATTN: J-3 STRATEGIC OPERS DIV

JOINT DATA SYSTEM SUPPORT CTR
ATTN: C-312 R MASON

JOINT STRAT TGT PLANNING STAFF
ATTN: JK (ATTN: DNA REP)
ATTN: JLAA
ATTN: JLKS
ATTN: JPEP

ATTN: JPPFD
ATTN: JPSS
ATTN: JPTM

NATIONAL SECURITY AGENCY
ATTN: B432 C GOEDEKE

DEPARTMENT OF THE ARMY

DEP CH OF STAFF FOR OPS & PLANS
ATTN: DAMO-RQC (C2 DIV)

HARRY DIAMOND LABORATORIES
2 CYS ATTN: SCHLD-NW-P
ATTN: SLCHD-NW-R R WILLIAMS

U S ARMY ATMOSPHERIC SCIENCES LAB
ATTN: SLCAS-AE-E

U S ARMY FOREIGN SCIENCE & TECH CTR
ATTN: DRKST-SD

U S ARMY NUCLEAR & CHEMICAL AGENCY
ATTN: LIBRARY

DEPARTMENT OF THE NAVY

OFC OF THE DEPUTY CHIEF OF NAVAL OPS
ATTN: NOP 941D
ATTN: OP 654/STRAT EVAL & ANAL BR
ATTN: OP 981N

THEATER NUCLEAR WARFARE PROGRAM OFC
ATTN: PMS-423317 (D SMITH)

DEPARTMENT OF THE AIR FORCE

AIR FORCE CTR FOR STUDIES & ANALYSIS
ATTN: AFCSA/SAMI (R GRIFFIN)
ATTN: AFCSA/SACC

AIR FORCE GEOPHYSICS LABORATORY
ATTN: CA/A STAIR
ATTN: LID/J RAMUSSEN
ATTN: LIS J BUCHAU
ATTN: LS
ATTN: LS/R O'NIEL
ATTN: LSI/ H GARDINER
ATTN: LYD/K CHAMPION

AIR FORCE TECHNICAL APPLICATIONS CTR
ATTN: TN

AIR FORCE WEAPONS LABORATORY, NTAAB
ATTN: NTN
ATTN: SUL

AIR UNIVERSITY LIBRARY
ATTN: AUL-LSE

DNA-TR-85-123 (DL CONTINUED)

DEPUTY CHIEF OF STAFF/AFROS
ATTN: AFROS (SPACE SYS & C3 DIR)

DEPARTMENT OF ENERGY

DEPARTMENT OF ENERGY
ATTN: DP-233

LAWRENCE LIVERMORE NATIONAL LAB
ATTN: J KNOX
ATTN: J PENNER
ATTN: L-31 R HAGER
ATTN: L-53 TECH INFO DEPT. LIBRARY

LOS ALAMOS NATIONAL LABORATORY
ATTN: D SAPPENFIELD
ATTN: R MALONE

SANDIA NATIONAL LABORATORIES
ATTN: D HARTLEY 8300

SANDIA NATIONAL LABORATORIES
ATTN: B ZAK
ATTN: TECH LIB 3141 (RPTS RECEIVING CLRK)

OTHER GOVERNMENT

CENTRAL INTELLIGENCE AGENCY
ATTN: OSWR/NED
ATTN: OSWR/SSD FOR K FEUERPFTL

DEPARTMENT OF DEFENSE CONTRACTORS

APPLIED RESEARCH CORP
2 CYS ATTN: A ENDAL

BDM CORP
ATTN: A VITELLO
ATTN: L JACOBS

INSTITUTE FOR DEFENSE ANALYSES
ATTN: E BAUER
ATTN: H WOLFHARD

KAMAN SCIENCES CORP
ATTN: E CONRAD

KAMAN TEMPO
ATTN: B GAMBILL
ATTN: DASIA
ATTN: R RUTHERFORD
ATTN: W McNAMARA

KAMAN TEMPO
ATTN: DASIA
ATTN: P ALDERSON

MISSION RESEARCH CORP
ATTN: G MCCARTOR

PACIFIC-SIERRA RESEARCH CORP
ATTN: E FIELD JR
ATTN: F THOMAS
ATTN: H BRODE, CHAIRMAN SAGE
ATTN: R SMALL

R & D ASSOCIATES
ATTN: F GILMORE
ATTN: M GROVER
ATTN: R TURCO

SCIENCE APPLICATIONS INTL CORP
ATTN: D BACON
ATTN: J COCKAYNE
ATTN: J MCGAHAN